ジョーンズ計算法とニューラルネットワークを用いた偏光光ファイバ歪みセンサシステムに関する研究

Muroran Institute of Technology

Doctoral Dissertation

Study on polarization optical fiber strain sensor system based on Jones calculus and neural networks

Name: Yao Zhao

Supervisor: Assoc. Prof. Shinya Sato

Division of Engineering

Abstract

Polarization sensors have attracted attention and been researched as they can be constructed with a very simple experimental setup. They utilize the polarization characteristic of light propagating in an optical fiber and determine the strain, stress, pressure, etc. from changes in the polarization state of light propagating in a single-mode optical fiber when the sensor is affected by external factors. However, in previous research, the use of either Hi-Bi fiber or polarization maintaining fiber made the cost of the sensor system very high and operate difficultly. In this work, we present a polarization sensor system that determines strains by measuring changes in polarization state in a single-mode fiber which are commercially available inexpensive fibers. This greatly reduces the cost of the sensor system. In the experiment, we use the fiber wound in a coil shape as a sensor. When strains are applied, the sensor is rotated by the invar wire that is attached to the sensor. Strains applied in the experiment can be determined from the measured polarization states when the sensor rotates.

In addition, we propose to calculate an arbitrary optical path using the Jones matrices of two rotated wave plates. The calculated polarization states obtained using the proposed method are in good agreement with the measured values, which demonstrated the feasibility of the proposed method. Therefore, when two Jones matrices representing the optical path are obtained, the polarization state of the transmitted light can be calculated from that of the reflected light on this optical path and vice versa. Also, the strains applied in the experiment are in good agreement with the calculated ones. These all verified the feasibility of the strain

sensor system developed in this work. Therefore, when the object (building, slope, etc.) connected to the other end of the invar wire is deformed, the strain amount can be obtained by this method. However, when a multipoint measurement is performed by connecting sensors in series, the size of the experimental data becomes enormous and it will become very difficult to use function fitting for data processing. Taking that problem into account, we performed data processing using a 3-layer feedforward neural network. The experimental data are used as training data for learning, that is, we take the measured polarization state as the input and the rotation angle of the sensor as the output for training the neural network. In addition, to test the trained neural network, we provided a newly measured polarization state to the trained network. The output of the trained network, namely, the rotation angle of the sensor, is almost the same as that applied in the experiment that generated the test data. These results demonstrate the feasibility of both the sensor system and the data processing methods proposed in the study.

Contents

1. Introduction 1

1.1 General Background 2

1.2 Research Purpose 3

1.3 Dissertation Outline 5

2. Optical Fiber Sensor 7

2.1 Fundamental of the Optical Fiber 8

2.2 Fundamental of Optical Fiber Sensors 10

2.3 Optical Fiber Sensing Method 12

2.3.1 Fiber Bragg Grating Sensor 12

2.3.2 Brillouin Optical Time Domain Reflectometry Sensor 13

2.3.3 Polarization Optical Fiber Sensor 14

3. Polarization Optical Fiber Sensor 16

3.1 Polarization 17

3.1.1 Types of Polarized light 17

3.1.2 Complex representation of electric field 19

3.1.3 Stokes parameters 20

3.2 Jones Calculus 21

3.3 Measurement Principle of the Sensor 23

3.4 Measurement Principle and Problems in Multipoint Measurement 25

4. Neural Network 28

4.1 Outline of Neural Network 29

4.2 Components and Forms of Network 30

4.2.1 Decisive 2-Value Model 31

4.2.2 Stochastic 2-Value Model 31

4.2.3 Decisive Analog Model 32

4.2.4 Architecture of Neural Network 35

4.3 Backpropagation Method 37

4.4 Design of Neural Network 42

5. Experiments and Results 46

5.1 Verification of twisting when rotating the sensor 47

5.2 Experiment using Jones calculus and Results 51

5.2.1 Experiment system 51

5.2.2 Experiment and results 53

5.2.3 Changes in the polarization state due to rotation of the sensor. 61

5.3 Experiment using a Neural Network and Results 67

6. Conclusions 75

6. Conclusions 76

Acknowledgments 79

References 80

1. Introduction

1.1 General Background

Natural disasters such as landslides and slope failures due to torrential rain, typhoons, and earthquakes frequently occur in recent years [1-4]. Disruption of transportation roads and collapse of houses due to such natural disasters has become a social problem, and disaster countermeasures are strongly demanded [5-32]. Therefore, it is becoming increasingly important to monitor social infrastructure such as roads, bridges, and tunnels in real time, to fully understand pre-disaster facts, to make correct decisions, and to take effective measures. This is expected to effectively reduce the damage caused by disasters. In addition, disasters often occur in wilderness and mountainous areas where natural conditions are severe.

Because of the vulnerability of these locations to lightning, rain, electromagnetic interference, etc., traditional electrical sensors are often easily damaged and may be difficult to monitor in real time. Since optical fiber sensors have features such as light weight, small size, insulation, and electromagnetic induction resistance, research for applying them to disaster prevention sensors is active. Since optical fiber sensors have features such as light weight, small size, electrical insulation, and resistance to electromagnetic induction, research on sensors that make use of these features is actively conducted, and development of measurement methods is in progress [31-51]. Among them, research for applying optical fiber sensors to disaster prevention sensors is also becoming increasingly active. The optical fiber sensor is not affected by electromagnetic interference because the sensor unit does not require a power supply. In addition, optical fiber sensors use silicon dioxide, so they have high corrosion resistance. This is a very important

aspect when setting up the sensor in the field especially where the environment conditions are very harsh.

When an optical fiber sensor is used for measurement, the characteristics (phase, frequency, wavelength, intensity, polarization, etc.) of light propagating through the optical fiber change when an external physical quantity is applied to the sensor unit [52-53]. By measuring the change in the properties of the light, it is possible to obtain an external physical quantity applied to the sensor. This is also the measurement principle of the optical fiber sensor. There are various types of optical fiber sensors depending on the measurement method. Among them, polarization sensors have attracted much attention and the development of the polarization sensors have been researched [54-61]. This is due to the fact that in addition to the properties of optical fiber sensors described above, the polarization sensors can be constructed with a very simple experimental setup. Therefore, there is a possibility that it can be applied to disaster prevention sensing systems such as tunnel failure, earthquake prediction, and strain survey of infrastructure.

1.2 Research Purpose

Optical fiber sensors have been widely used for sensing and monitoring in various engineering fields because of their superiority to electrical sensors as described previously. They are used to measure various physical quantities such as strains, temperatures, pressures, current, vibration, displacement, and so on. Among many types of optical fiber sensors, there is also an increasing number of studies on polarization optical fiber sensors that exploit the properties of the state of polarization of light as a measurement method. This is because the polarization

optical fiber sensors can be built with a simple structure compared with other sensing methods. When external influences are directly or indirectly applied to the sensor, the polarization state of the light propagating in the fiber of the sensor system changes. By measuring the change in the state of polarization, it is possible to detect the external influences applied to the sensor. However, in previous studies, polarization optical fiber sensor systems have used high birefringence or polarization maintaining fibers for measurement [59]. The use of these fibers not only makes the cost of the sensor system very expensive but also makes it difficult to operate. These also limit to some extent the development and spread of polarization optical fiber sensors. Therefore, we decided to develop a small size, low-cost polarization fiber sensor system which can be used to measure strains. In the experiment, since a commercially available low-cost single mode optical fiber is wound as a coil and used as a sensor, the cost is greatly reduced compared to the conventional polarization optical fiber sensor.

In the experiment, we rotated the sensor by pulling an invar line connected to the sensor. This is conducted to simulate the generation of strain with the movement of the Invar line. That is, the strain is applied by pulling the invar line. As the sensor rotates, changes in the state of polarization of light are measured by the polarization analyzer. Since the measured polarization state corresponds to the movement distance (strains) of the invar line, the distance of the invar line can be determined from the measured polarization state. In this way, when the building or the slope connected to the other end of the Invar line is deformed, the strains of the measured object can be obtained by this measurement method. Furthermore, the sensor system developed in this study is not affected by

external temperature changes and does not require temperature compensation.

In addition, the ultimate goal of this study is to connect multiple sensors in series on a single fiber for multi-point measurement of strain. However, there is a problem with multi-point measurement, which is the effect of the front-end sensor on the rear-end sensor. Once the first sensor has rotated, the light entering the second sensor will change even if the second sensor does not rotate. Then, the measurement result for the second sensor will have an error. To solve this problem, we propose to use the Jones matrices of two rotated wave plates to represent an arbitrary optical path, so that we can calculate the polarization state of the incident light entering the second sensor, even if the first sensor rotates. In addition, in order to solve the problem of large data processing when the multipoint measurement is performed, we also propose the use of neural networks for data processing. In this study, we use a three-layer feedforward neural network for data processing.

1.3 Dissertation Outline

As described above, the introduction, i.e. Chapter 1, describes the general background, research purpose, and dissertation outline.

Chapter 2 presents an overview of optical fibers and optical fiber sensors. The concept, characteristics, and several sensing methods of optical fiber sensors are described here.

Chapter 3 presents the outline of polarized light, Jones calculus, and the measurement principle of polarization optical fiber sensors. In addition, we describe the multipoint strain measurement principle based on the proposed sensor system and the problems in multipoint measurement experiment.

Chapter 4 describes the outline, components, and structure of neural networks. In addition, the back propagation method, and the design of the neural network in this study are also described in this chapter.

Chapter 5 presents the experiment and experimental results. The experiment includes two parts. One is to verify the proposed method that an arbitrary optical path can be computed using the Jones matrices of two rotated wave plates. The other one is also the strain measurement experiment, however, this time we performed the data processing using a 3-layer feed-forward neural network. The experiment, data processing method, and the results are presented in this chapter, showing the feasibility of the proposed sensor system.

Finally, the conclusions drawn from this study are given in chapter 6.

2. Optical Fiber Sensor

2.1 Fundamental of the Optical Fiber

Optical fibers are flexible, thin thread-like transparent material made of quartz glass or plastic, through which optical signals pass. Nowadays, optical fibers are being drawn to the home, making them indispensable for optical communications. In addition, by taking advantage of the characteristics and structure of optical fibers, they are also used for various applications such as sensors, fiber lasers, high power light guides and the like [62-63]. The basic construction of an optical fiber is a two-layer structure consisting of a core in the center and a cladding material surrounding the core. The main component of the optical fiber core material is silicon dioxide, and a very small amount of dopants is used to increase the refractive index of the core. In this way, the fiber core has a higher refractive index than the cladding [64]. The general structure of an optical fiber is shown in Fig 2.1.1.

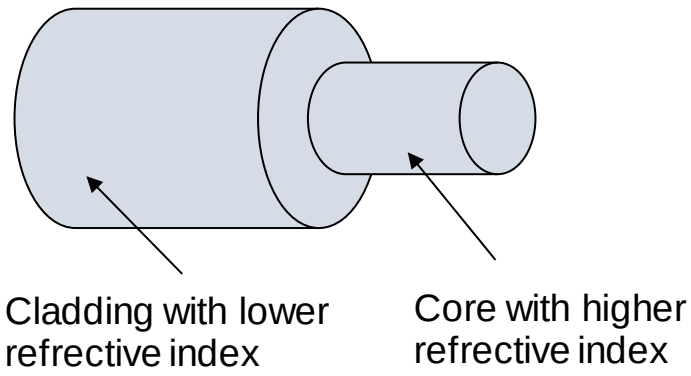

Fig.2.1.1. Structure of an optical fiber.

As previously described, the fiber core is doped with impurities in order to increase the refractive index of the core. This is done to take advantage of the total reflection of light in order to confine the optical signal inside the core of the

fiber for long distance transmission. As long as we adjust the angle at which light is incident into the core of the fiber, we can ensure that light is totally reflected at the boundary of the fiber core and the cladding and is transmitted through the fiber. Total internal reflection is also a necessary condition to transmit optical signals using an optical fiber. Only then can the optical signal be completely confined within the core of the optical fiber for propagation, thereby avoiding unnecessary signal losses. It is necessary to ensure that optical signals propagate within the fiber core not only in the field of communications but also in the field of fiber sensing. Typically, the core has a refractive index of 1.47 and the cladding has a refractive index of 1.46. The propagation of the optical signal in the core of the fiber using total internal reflection is shown in Fig.2.1.2 [65].

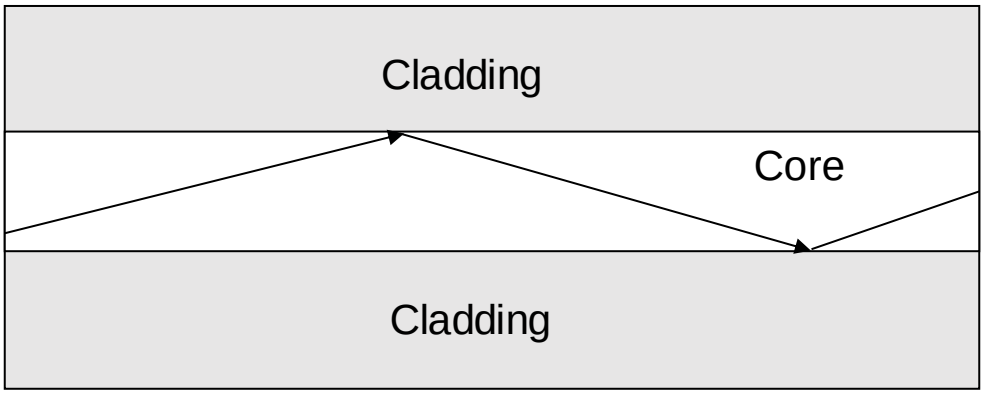

Fig. 2.1.2. Propagation of light in the fiber core.

Optical fibers are roughly classified into multimode optical fibers (MMF) and single-mode optical fibers (SMF) depending on the propagation mode. Multimode optical fiber is one designed to carry from hundreds to thousands of light rays or propagation modes, each at a slightly different reflection angle within the optical

core. Multimode optical fibers generally have a wider core diameter, typically 50-100 micrometers. And multimode optical fibers are mostly used for communication over relatively short distances because of the large inter-mode dispersion of multimode fiber, resulting in narrow fiber bandwidth. On the other hand, single mode optical fiber has only one propagation mode, and it has no inter-mode dispersion, so the bandwidth is very wide. Therefore, it is best to use single-mode fiber with very wide bandwidth for high speed and long distance transmission systems. In this study, single-mode fibers are used to implement the experiments.

2.2 Fundamental of Optical Fiber Sensors

In recent years, with the development of optical fiber communication technology, laser light source technology, and optical fiber sensing technology, optical fiber sensors have been vigorously researched and developed in the past decades. One important reason is that the fibers that make up the fiber optic sensor have many unique features and advantages, which are described as follows [66]:

(a) thin diameter

(b) lightweight

(c) flexibility

(d) non-inductive

(e) corrosion resistance

(f) explosion proof

These features are very useful for installation and construction even in a narrow space that is not easily accessible, and in transportation equipment where

exercise performance and transport efficiency are important. Although traditional electrical sensors are widely used in many fields, the measurement unit always requires a power supply which is susceptible to lightning and surge current. This is a serious problem that is urgent to be solved. In addition, if there are electronic and electrical devices nearby, sensors and measures that do not receive electromagnetic induction are required. The advantages of the aforementioned optical fibers have enabled fiber optic sensors to successfully solve the problems faced by these electrical sensors.

Nowadays, optical fiber sensors are playing an increasingly important role in modern life and industry and are currently being studied to be more sensitive, more precise and more adaptable. They have been widely used for measuring physical, biological, and chemical parameters in various fields. An optical fiber sensor measures external changes by detecting changes in light properties such as intensity, phase, frequency, and polarization. The optical fiber sensor basically consists of a light source, an optical fiber as a transmission path, measurement equipment and an optical receiver. However, from the specific role of the fiber in the sensing system, the sensor is generally divided into two types [67]. That is to say, in the fiber sensor system, the fiber is used only as a transmission path, or the fiber itself is used as a sensor. The first is that there are sensor components in the sensing system, and the fiber is only used as a transmission path. The second is that the fiber itself is used as a sensor, and the external action is applied directly to the fiber. In this research, we conduct experiments with the optical fiber itself as a sensor. This kind of optical fiber sensor has very unique features and characteristics, which include: small size, lightweight, flexibility, immune to

electromagnetic induction, corrosion resistance, and distribution and quasi-distribution measurement [31-32]. These characteristics and features allow the use of fiber optic sensors in places where traditional electrical sensors cannot apply, such as the places where there is electromagnetic interference or where thunderstorms occur frequently. In this study, the state of polarization of light propagating in optical fibers will change when external changes are applied to the sensor, therefore, we can measure the changes in the state of polarization of light to determine the external changes that are applied to the sensor.

2.3 Optical Fiber Sensing Method

There are various methods of fiber sensing, and they all have their own characteristics. When we want to choose a sensing method, we need to have a good understanding of how this method works. On the basis of understanding the principle and selecting for your own measurement target, satisfactory measurement results will be obtained. Here, we mainly introduce fiber sensing methods based on three measurement principles. The first is the fiber Bragg grating (FBG) detection method that reflects a specific wavelength, the second is the Brillouin Optical Time Domain Reflectometry (BOTDR) detection method using backscattered light, and the third is the polarization detection method used in this study.

2.3.1 Fiber Bragg Grating Sensor

FBG is made by irradiating a doped fiber with a strong laser to change the refractive index of the fiber core. The refractive index of the fiber will change correspondingly with the spatial distribution of the luminous intensity. The fiber core after strong laser irradiation has a periodic change in refractive index and

becomes a fiber grating. An FBG reflects only a specific wavelength called the Bragg wavelength λ_B and transmits the other wavelengths when Ithe ight is incident to the FBG [34]. The Bragg wavelength λ_B can be expressed by Eq. (2.3.1).

$$\lambda_B = 2n\Lambda \qquad (2.3.1)$$

In the equation, n is the effective refractive index and Λ is the grating period. When strain or temperature is applied to the FBG, both n and λ change and the Bragg wavelength shifts. Since the shift of the Bragg wavelength has a linear relationship with the change in temperature and strain, the temperature and strain applied to the FBG can be detected by observing the shift of the Bragg wavelength.

As described above, an FBG sensor is not only sensitive to changes in temperature but also sensitive to temperature changes. It is therefore often used as a strain sensor and temperature sensor to measure strain and temperature changes. This also means that temperature compensation must be performed when measuring strain using FBG sensors.

2.3.2 Brillouin Optical Time Domain Reflectometry Sensor

When an optical pulse is incident on an optical fiber, it generates various scattered light. The scattered light that returns to the light incident end is called backscattered light. There are various types and characteristics of scattered light, one of which is called Brillouin scattered light depending on strain and temperature changes. Brillouin scattered light has a feature that the frequency distribution of Brillouin scattered light generated in that part changes due to strain or temperature change applied to the optical fiber. That is, when the strain or

temperature change is applied to the optical fiber, the frequency of the Brillouin scattered light will shift. Since the Brillouin frequency shift amount changes linearly with respect to strain and temperature, measuring this shift amount enables detection of strain or temperature change applied to the optical fiber [68]. In this method, since the optical fiber itself is a sensor, linear and planar measurement and monitoring that cannot be realized by conventional measurement have become possible. Another advantage of the BOTDR measurement system is that it can measure continuous distribution for several tens of kilometers from one end of a single optical fiber [69]. Furthermore, if the sensor optical fiber is installed in a loop, measurement can be continued by measuring from both ends even if there is a break at one place.

However, since the Brillouin scattered light signal returning to the incident end is low, it is necessary to perform averaging processing. Therefore, it takes tens of minutes for one measurement. This also means that real-time dynamic measurements are not possible with BOTDR sensor systems.

2.3.3 Polarization Optical Fiber Sensor

The polarization optical fiber sensor is a sensor that detects the amount of strains by measuring the changes in the polarization states when strains are applied to the sensor. In principle, it is possible to connect multiple sensors on one fiber, so multipoint measurement can be implemented with one optical measurement instrument. Slope installation is simpler than conventional types because polarization is less susceptible to loss of fiber connections and connectors can be used for installation and extension. Therefore, it is expected to reduce installation cost. In this study, the fiber used as a sensor does not

require any special treatment, and the experiment can be completed using commercially available single-mode fiber. Compared to studies using birefringent fibers or highly polarization maintaining fibers, we can achieve lower prices. The detailed description of polarization optical fiber sensors will be presented in Chapter 3.

3. Polarization Optical Fiber Sensor

3.1 Polarization

Light is an electromagnetic wave whose vibration direction is perpendicular to the propagation direction. Light in which an electric field and a magnetic field vibrate only in a regular direction in this plane is called polarization. Random light with no regularity in the polarization of light waves is called natural light [70]. The polarized light can change shape freely without losing energy or increasing entropy. Also, since polarized light is the simplest light, it can be handled physically briefly, and mathematical handling for experimental prediction can be easily done [71-72]. From such a perspective, polarized light is easier to handle than natural light. Cross-sectional views are often used to represent polarized light. The sectional view is the trajectory of the tip of the electric field vector when the observer stands on the path of the light ray and looks toward the light source at the origin of the coordinate.

3.1.1 Types of Polarized light

When considering the electric field of plane polarized light traveling in the Z direction, let each component E_x and E_y be expressed as:

$$\left.\begin{aligned} E_x &= A_x \cos(\omega t - kz + \delta_x) \\ E_y &= A_y \cos(\omega t - kz + \delta_y) \end{aligned}\right) \qquad (3.1.1)$$

The polarization state is determined by the amplitude ratio $\mathrm{A_x/A_y}$ and the phase difference $\delta = \delta_y - \delta_x$ [73].

(a) Elliptically polarized light

If $A_x \neq A_y$ and it is an arbitrary phase difference δ which is shown in Eq. (3.1.1), the locus of the tip of the electric field vector is

$$\left(\frac{E_x}{A_x}\right)^2+\left(\frac{E_y}{A_y}\right)^2-2\frac{E_xE_y}{A_xA_y}\cos\delta=\sin^2\delta \qquad (3.1.2)$$

and it will draw an ellipse. This polarized light is called elliptically polarized light, and the cross-sectional view is shown in Fig. 3.1.1 (a). The inclination angle α between the major axis of the ellipse and the x-axis is shown as

$$\tan 2\alpha=2\frac{A_xA_y}{A_x^{\,2}-A_y^{\,2}}\cos\delta \qquad (3.1.3)$$

The rotation direction of the electric field is counterclockwise when 0 <δ <π, and clockwise when −π<δ <0. Common polarized light is elliptically polarized light and it becomes circularly polarized light and linear polarized light when special conditions are met.

(b) Circularly polarized light

If $A_x=A_y$ and $\cos\delta=0$ in Eq. (3.1.1), the polarized light is called circular polarized light. The cross-sectional view is shown in Fig. 3.1.1 (b). The determination of the direction of rotation is the same as in the case of elliptically polarized light

(c) Linearly polarized light

If $A_x=A_y$ and $\cos\delta=1$ in Eq. (3.1.1), the polarized light is called linearly polarized light. The cross-sectional view is shown in Fig. 3.1.1 (c). The inclination (orientation angleϕ) from the x-axis of the oscillating plane of the electric field is shown as

$$\phi=\tan^{-1}\left(\frac{E_y}{E_x}\right) \qquad (3.1.4)$$

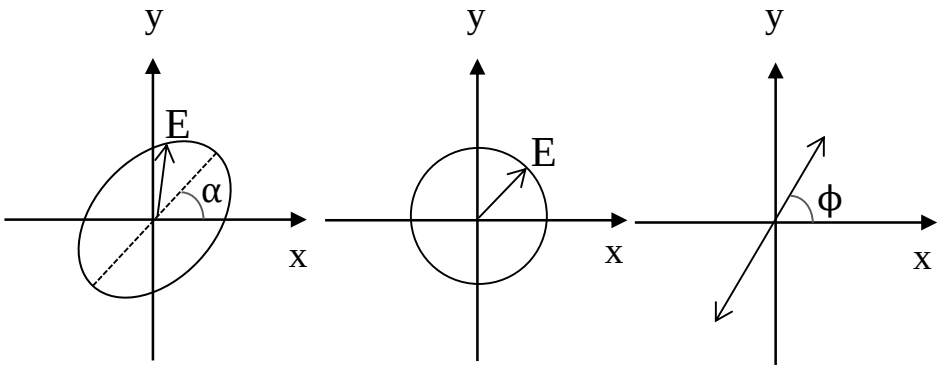

(a) Elliptically polarized light (b) Circularly polarized light (c) Linearly polarized light

Fig. 3.1.1. Types of Polarized light

3.1.2 Complex representation of the electric field

Since the equation of the electric field can be expressed in the complex form, Eq. (3.1.1) can be rewritten to the complex form as [73]

$$\left.\begin{aligned} E_x &= A_x e^{i(\omega t - kz)} \\ E_y &= A_y e^{i(\omega t - kz + \delta)} \end{aligned}\right\} \qquad (3.1.5)$$

Shifting the phase reference $-\delta/2$

$$\left.\begin{aligned} E_x &= A_x e^{i(\omega t - kz - \frac{\delta}{2})} \\ E_y &= A_y e^{i(\omega t - kz + \delta + \frac{\delta}{2})} \end{aligned}\right\} \qquad (3.1.6)$$

Since the polarization state is determined by the ratio of the amplitude and the phase difference, spatial and temporal changes can be ignored. Eq. (3.1.6) can be represented as

$$\left.\begin{aligned} E_x &= A_x e^{-i\frac{\delta}{2}} \\ E_y &= A_y e^{i\frac{\delta}{2}} \end{aligned}\right\} \qquad (3.1.7)$$

3.1.3 Stokes parameters

In the previous section, the polarization state is expressed using the amplitude and phase of light, but it is not easy to measure the amplitude and phase of light when measuring the polarization state. When actually making measurements, use Stokes parameters as light intensity. The Stokes parameters consist of four terms S_0, S_1, S_2 and S_3. From S_0, the intensity of the entire light, the intensity of the horizontal linear polarization component, the intensity of the + 45 ° linear polarization component, and the intensity of the right circular polarization component are respectively shown. If temporal changes of the polarization state can be ignored and the complex conjugate is * [73-74], the Stokes parameter can be defined as

$$\left.\begin{aligned} S_0 &= E_x E_x^* + E_y E_y^* = A_x^2 + A_y^2 \\ S_1 &= E_x E_x^* - E_y E_y^* = A_x^2 - A_y^2 \\ S_2 &= E_x E_y^* + E_y E_x^* = 2A_x A_y \cos\delta \\ S_3 &= E_x E_y^* - E_y E_x^* = 2A_x A_y \sin\delta \end{aligned}\right\} \qquad (3.1.8)$$

Completely polarized light is shown as

$$S_0^2 = S_1^2 + S_2^2 + S_3^2 \qquad (3.1.9)$$

In many cases, standardized Stokes parameters are used in which each polarization component of S_1 to S_3 is standardized by the overall intensity S_0. The phase difference can be obtained by Eq. (3.1.10).

$$\delta = \tan^{-1}\left(\frac{S_3}{S_2}\right) \qquad (3.1.10)$$

The Stokes parameters and the electric field representations are interrelated and can be converted to each other by Eq. (3.1.8) and Eq. (3.1.10). In this experiment, the polarization state is handled by converting the Stokes

parameters obtained by the polarization analyzer into the electric field display.

3.2 Jones Calculus

As described above, polarization represents a state in which the electrical field vibration of a plane of light is spatially biased [73-74]. When the electrical field is represented by $\mathbf{E}$, then the arbitrary polarization can be represented by a vector sum of two fundamental polarized lights E_x and E_y The parameters for determining the polarization state is the phase difference δ of E_x and E_y , and the ratio of the amplitudes of E_x and E_y.

There are two methods for calculating the polarization of an optical path, the Jones matrix calculus, and the Mueller matrix calculus [75-76]. Since completely polarized light is used in the experiment, for each optical element we decided to use the Jones matrix as it is easier to calculate than the Mueller matrix. The Jones matrix calculus is a method of representing polarized light by a matrix. It is composed of a 2×1 Jones vector which represents an electrical field component, and a 2×2 Jones matrix representing the polarization component. Using complex notation, the 2×1 Jones vector representing the electric field is expressed as:

$$\mathbf{E}=\begin{bmatrix}\mathrm{E}_x\\ \mathrm{E}_y\end{bmatrix}=\begin{bmatrix}\mathrm{E}_{0x}exp\{i(wt-kz+\delta_x)\}\\ \mathrm{E}_{0y}exp\{i(wt-kz+\delta_y)\}\end{bmatrix}=exp[i(wt-kz)]\begin{bmatrix}\mathrm{E}_{0x}exp(i\delta_x)\\ \mathrm{E}_{0y}exp(i\delta_y)\end{bmatrix} \quad (3.2.1)$$

For actual measurements, only the phase difference is taken into account, so Eq. (3.2.1) can be rewritten using a phase difference while omitting $exp[i(wt-kz)]$ as shown in Eq. (3.2.2) [32].

$$\mathbf{E}=\begin{bmatrix}\mathrm{E}_{0x}exp(i\delta_x)\\ \mathrm{E}_{0y}exp(i\delta_y)\end{bmatrix}=\begin{bmatrix}\mathrm{E}_{0x}\\ \mathrm{E}_{0y}exp(i\delta)\end{bmatrix} \quad (3.2.2)$$

$$\delta=\delta_y-\delta_x \quad (3.2.3)$$

where E_{0x} and E_{0y} are amplitudes, δ_x and δ_y are phases, i=$\sqrt{-1}$, and δ is the phase difference. A polarization element is represented by a 2×2 Jones matrix $\mathbf{J}$, which is shown as:

$$\mathbf{J} = \begin{bmatrix} j_{11} & j_{12} \\ j_{21} & j_{22} \end{bmatrix} \tag{3.2.4}$$

When the optical element receives an incident light represented by the Jones vector $\mathbf{E}_{in}$, it changes the polarization state of the incident light to emit a new polarization state vector $\mathbf{E}_{out}$. The polarization conversion process by the optical element is expressed by [32]:

$$\mathbf{E}_{out} = \mathbf{J} \cdot \mathbf{E}_{in} \tag{3.2.5}$$

In addition, when there are M optical elements, we can use Eq. (3.2.6) expressed below to calculate the transmitted light through multiplying the Jones matrices representing the optical elements in order from right to left [32].

$$\mathbf{E}_{out} = \mathbf{J}_{M-2} \cdot \mathbf{J}_{M-1} \cdot \mathbf{J}_2 \cdot \mathbf{J}_1 \cdot \mathbf{E}_{in} \tag{3.2.6}$$

However, in practical applications, we can only use this method after obtaining the Jones matrices of all optical elements in the optical path. It is often very difficult to obtain the Jones matrices of all optical elements in the optical path. Therefore, we propose to use the Jones matrices of two rotated wave plates to calculate an arbitrary optical path. Thus, no matter how many optical components are included in the optical path, we can determine the polarization state of the transmitted light from the polarization state of the incident light of the optical path as long as we can find the Jones matrix of the two rotated wave plates representing the optical path. This calculation can be expressed by Eq. (3.2.7).

In addition, the Jones matrix of an arbitrarily rotated wave plate is expressed by Eq. (3.2.8) [77], which is a regular matrix.

$$\mathbf{E}_{out} = \mathbf{J}_2 \cdot \mathbf{J_1} \cdot \mathbf{E}_{in} \tag{3.2.7}$$

$$\mathbf{J}_2, \mathbf{J}_1 = \begin{bmatrix} \cos\frac{\phi}{2} - i\sin\frac{\phi}{2}\cos 2\theta & -i\sin\frac{\phi}{2}\cos 2\theta \\ -i\sin\frac{\phi}{2}\cos 2\theta & \cos\frac{\phi}{2} + i\sin\frac{\phi}{2}\cos 2\theta \end{bmatrix} \tag{3.2.8}$$

where $\emptyset$ represents the phase difference of the arbitrarily rotated wave plate, and θ represents the orientation angle.

3.3 Measurement Principle of the Sensor

As shown in Fig. 3.3.1, the sensor that is used in the experiment is a single-mode 8.3/125 fiber that is wound in a circle shape [31]. When the fiber is wound into a circle, the core and cladding of the fiber are usually deformed, thereby changing the fast axis refractive index and the slow axis refractive index. Birefringence in the fiber is caused by changes in the fast and slow axis refractive indices. The influence of this birefringence can be increased depending on the size of the winding radius to be integrated from end to end of the wound portion of the optical fiber. By adjusting the number of turns and the winding radius of the optical fiber, it is possible to have the same performance as a wave plate. In other, the circularly wound fiber can be used as a wave plate. The phase difference, which is expressed as δ, of the wound part can be calculated by [31]:

$$\delta = \frac{2\pi}{m} \tag{3.3.1}$$

$$m = \frac{\lambda}{2\pi a r^2}\frac{R}{N} \tag{3.3.2}$$

where *N* is the number of turns of the fiber; *r* is the cross-sectional radius of the

fiber; R is the bending radius of the fiber; λ is the wavelength of the laser light; and a is calculated to be 0.13 [78]. In the experiment, N is set to 1, R to 0.0215 m, r to 6.25×10^{-5} m, and λ to 1.55×10^{-6} m. Then we substituted these values into Eq. (3.3.1) and (3.3.2) and calculated the phase difference of the sensor to be 34.43°. The orientation angle of the sensor was the actual rotation angle of the sensor applied in the experiment.

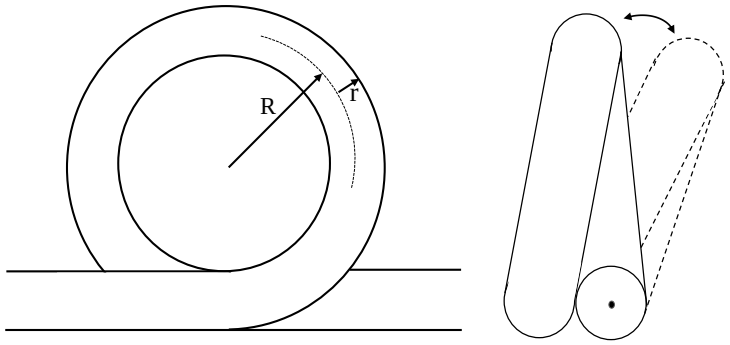

(a)

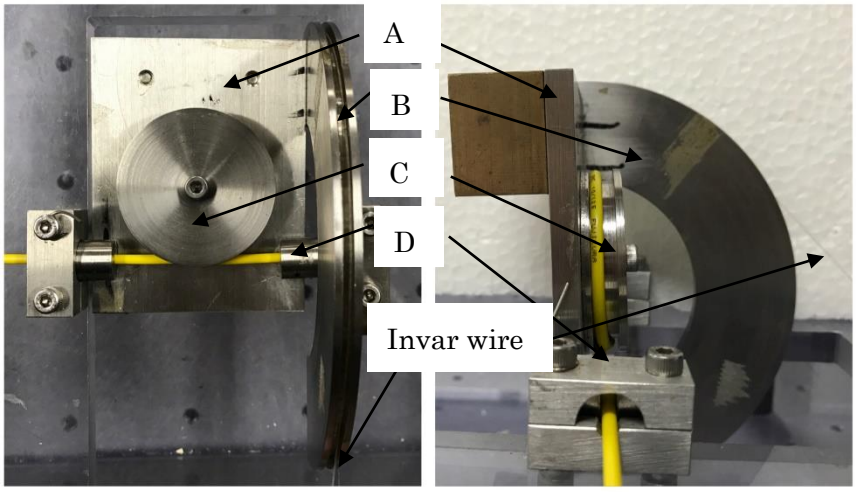

(b)

Fig. 3.3.1. Schematic diagram of the sensor.

Figure 3.3.1(b) shows the actual photo of the sensor part, including a top view and a left view. The base (A) with a sector part (B) is rotatable, and the radius of

the sector part is donated as R'. And, we fixed the cylinder (C) with a radius of 0.02m to the base using screws. Then, the optical fiber wound around this cylinder was used as a sensor and is fixed in the fixing slots (D) [32]. In the experiment, the Invar wire was attached to the sector part. When we pull the Invar wire to rotate the base, the sensor will also rotate with it. Then, we can use the rotation angle of the sensor to calculate the movement distance of the Invar wire, and further determine the strains applied in the experiment. Since the rotation angle of the sensor is obtained from the measured polarization state in the experiment, determining the strains applied through measuring the polarization state is possible. Here, the strain, which is denoted as ε, is defined as the percentage ratio between the movement distance ΔL of the invar wire and the length L (1 m) of the invar wire, which are expressed as [32]

$$\Delta L = \pi R' \frac{\rho}{180}, \tag{3.3.3}$$

$$\varepsilon = \frac{\Delta L}{L}, \tag{3.3.4}$$

where R' is 0.065 m and ρ (∘) is the rotation angle of the sensor.

3.4 Measurement Principle and Problems in Multipoint Measurement

In practical applications, there are many occasions where multipoint monitoring and measurement of strains is required. Based on the strain measurement system proposed in this study, multipoint measurement of strains can be performed using the time delay of reflected pulses from sensors when they are connected in series. However, in multi-point measurement, there is a problem that the front-end sensor affects the rear-end sensor. However, in multipoint measurement of strains, the problem arises that the front-end sensor affects the

rear-end sensor. Here, we take the two sensors connected in series as an example to illustrate the problems encountered in multipoint measurement. When the first sensor rotates, the polarization of the transmitted light from it changes, which directly causes the polarization of the incident light entering the second sensor to change. This also causes the polarization state of the reflected light from the second sensor measured in the experiment to change, even if the second sensor does not rotate. In addition, in the multipoint strain measurement experiment, once all the sensors are connected, we cannot separately measure the transmitted light from each sensor or the incident light entering each sensor. The polarization states of the reflected light from each sensor are the only parameters we can measure. If we can calculate the polarization state of the incident light incident entering the second sensor, and based on the measured polarization state of the reflected light of the second sensor, we can correctly obtain the rotation angle of the second sensor. That is, if we can correctly calculate the polarization state of the incident light entering each sensor in the multipoint experimental system, multipoint strain measurement can be implemented. However, in the present experiment, the polarization state of the incident light of each sensor could not be correctly calculated by the original calculation method. Therefore, as mentioned earlier, we propose to use the Jones matrices of two rotated wave plates to represent an arbitrary light path. Then, regardless of whether the first sensor is rotated, we can correctly determine the polarization state of the incident light entering the second sensor as long as we find the Jones matrices representing the optical path. The calculated value of the polarization state of the incident light entering the second sensor is then used

instead of its actual value. In this way, we believe that the problem of the influence of the first sensor on the sensor sensor in multipoint strain measurement can be solved. This method is also applicable when there are three or more sensors. As can be seen from the foregoing, when the sensor is rotated, we measure the polarization state of the reflected light from the sensor, represented by three Stokes parameters. That is, one rotation angle will correspond to three Stokes parameters. In the multipoint strain measurement experiment, two or more sensors will be connected, and the experimental data will become very large. It will take time to calculate the rotation angle of the sensors from the polarization states of each sensor because the polarization state of the reflected light of each sensor cannot be calculated at the same time. Moreover, an error has already occurred in the calculation of the polarization state, and it is possible to generate a larger error when using the calculated values of the polarization state to obtain the rotation angle of the sensor. Therefore, we use neural networks for data processing in our research because neural networks have the ability to handle multiple inputs and multiple output problems. As long as we design the neural network we need, we can get the rotation angle of each sensor at the same time. This not only saves a lot of time but also improves the accuracy of data processing. The detailed description of the neural network will be introduced in Chapter 4.

4. Neural Network

4.1 Outline of Neural Network

A neural network is a mathematical model established by abstracting the human brain neuron network from the perspective of information processing. In engineering applications, it is commonly referred to as an artificial neural network. Neural networks can effectively approach a wide range of applications. In particular, it exhibits excellent capabilities in the problems of pattern mapping, pattern perfection, pattern classification and the like. The first research on neural networks information processing is the model of neurons proposed by McCulloch and Pitts in 1943 [79]. They described the concept of neurons in their research, which are the units that exist in the network, mainly accepting input, processing input, and producing output. A neural network is a network constructed by mutually connecting artificial elements simulating nervous system cells (neurons) of a living body, and has three major features [80-82].

The first characteristic is "nonlinearity". It is well known that neural networks have powerful approximation capabilities and can achieve high precision approximation for any complex function. The reason for this ability is the nonlinear nature of the network. With the linear activation function, the neural network simply combines the input and outputs it again, so the approximation of complex functions cannot be achieved. With nonlinear activation functions, neural networks can approach complex functions at will.

The second characteristic is "learning ability", which is also said to be the greatest attraction of neural networks. Learning ability is the ability to automatically form the necessary functions based on the examples presented. This ability is suitable for problems that cannot be solved by conventional

methods. In a system with learning ability, it is not necessary to design the mechanism artificially.

The third feature is "parallelism". A neural network is one of the realizations of massively parallel computers, and a theoretical system for systematically grasping parallel operation has been established.

4.2 Components and Forms of Network

A neural network is a network that simulates the human brain neurons in order to realize artificial intelligence-like machine learning technology. It is a model established from the abstraction of specific functions of the human brain neuron network from the perspective of information processing. A neuron model is a model that contains inputs, outputs, and computational functions, much simpler than the actual neurons of a human brain. In a neural network, a neuron is the basic unit of computation. It accepts external inputs or inputs from other neurons and produces outputs after computation. There are several different models of neurons depending on the method of computation, and we need to choose the appropriate model based on the characteristics of our experimental data. When deciding the model of a neuron, it is generally considered from two aspects [80]. The first one is the operation of the element is " decisive " or "probabilistic". The other is whether the output is "2 -value" or "analog". Currently, neural network engineering models that most used in neural networks include decisive 2-value models, stochastic 2-value models, and decisive analog models. In our experiments, the polarization state is an analog value that is critical to the rotation angle. Therefore, this study uses a "Decisive analog model". The neuron model and the activation function used are described as follows.

4.2.1 Decisive 2-Value Model

The decisive 2-value model is modeled by a decisive element with a 2-value output of {0, 1} corresponding to whether the neuron is excited or not [80-82].

We assume the signal input to the model to be {$x_1, x_2 \ldots x_N$}. By multiplying these inputs by weights {$w_1, w_2 \ldots w_N$} and adding them together, an amount s corresponding to the intracellular potential is obtained. Here, the weights correspond to the synaptic connection weights. If s exceeds the threshold θ, the output y will be 1, otherwise, the output y will be 0. The calculation is shown in Eq. (4.2.1) and Eq. (4.2.2). And, the decisive 2-value model is shown in Fig. 4.2.1.

$$s = \sum_{n=1}^{N} w_n x_n \tag{4.2.1}$$

$$y = \begin{cases} 1 & s \geq \theta \\ 0 & s \leq \theta \end{cases} \tag{4.2.2}$$

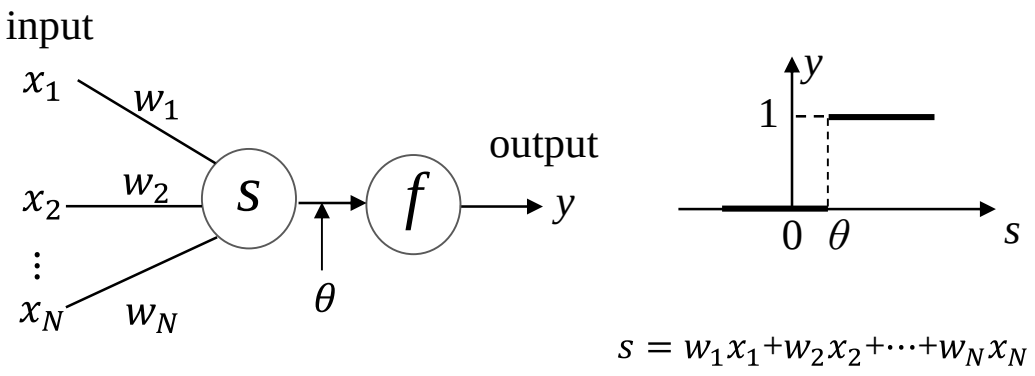

Fig. 4.2.1 Decisive 2-value model.

4.2.2 Stochastic 2-Value Model

A stochastic 2-Value Model is a model to decide stochastically whether to set this output valued to either {0, 1}, which is shown in Fig. 4.2.2. That means even if the input is the same, the output may take different values [80-82].

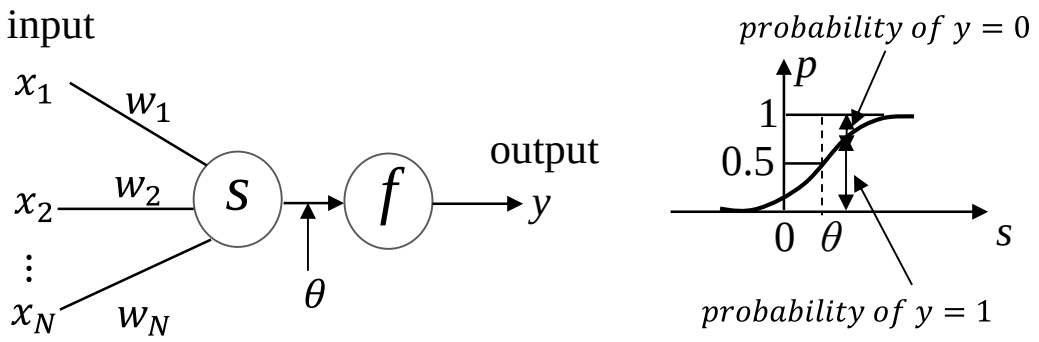

$$s = w_1x_1 + w_2x_2 + \cdots + w_Nx_N$$

Fig. 4.2.2. Stochastic 2-value model.

The intracellular potential s is calculated from the input in the same way as the decisive model. Then, calculate the sigmoid function value p for s, and set the output y to 1 with the probability of p, and 0 with the probability of 1-p. The calculation is expressed by Eq. (4.2.3) to Eq. (4.2.6) [80-82].

$$\mathrm{s} = \sum_{n=1}^{N} w_n\, x_n \tag{4.2.3}$$

$$\mathrm{p} = \mathrm{sigmoid}(\mathrm{s} - \theta) \tag{4.2.4}$$

$$\mathrm{P}(y = 1) = \mathrm{p} \tag{4.2.5}$$

$$\mathrm{P}(y = 0) = 1 - \mathrm{p} \tag{4.2.6}$$

4.2.3 Decisive Analog Model

A decisive analog model is a model that determines the output *y* as an analog value in the range of $0 \le \mathrm{y} \le 1$ and definitely determines this output from the input. The intracellular potential s is obtained by the same procedure as the 2-value mode described above. However, different from the decisive 2-value model, the continuous output will be obtained by using a function called a sigmoid

function when calculating y from s. The sigmoid function is shown in Fig. 4.2.3, and its equation is expressed as Eq. (4.2.7) [80-82].

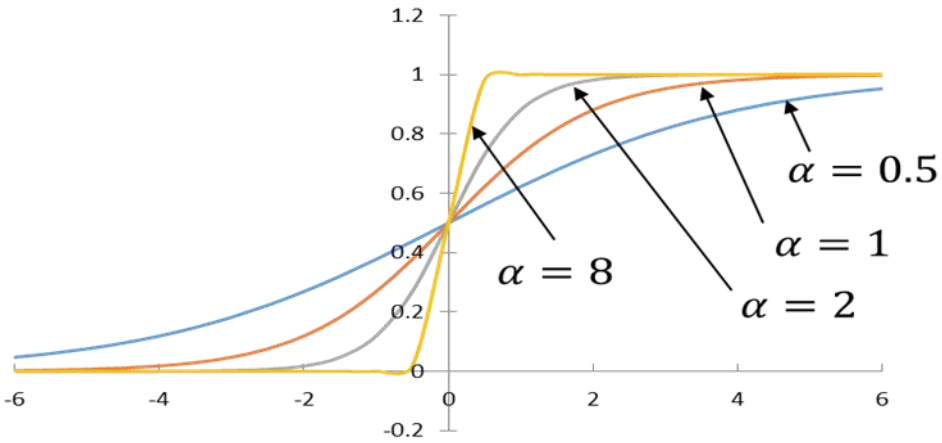

Fig. 4.2.3. Sigmoid function.

$$\text{sigmoid}(z) = \frac{1}{1+e^{-\alpha z}} \tag{4.2.7}$$

It is an important function representing input/output characteristics of neurons. In Eq. (4.2.7), α is a coefficient which is called gain. The output of the Sigmoid function is a continuous value, and the Sigmoid function is a monotonic function for the input, usually used for backpropagation method. The sigmoid function and its derivative are also continuous. Also, as shown in Fig. 4.2.3, the sigmoid function approaches the step function if the gain of the sigmoid function is increased. Conversely, when the gain is larger than 0 and sufficiently smaller than 1, the sigmoid function becomes a linear function. This requires us to set the initial value of the gain, neither too large nor too small, but to choose a suitable initial value.

As shown in Fig. 4.2.3, the function rises with z=0 as a boundary, and when the threshold is θ, the function can be shifted to the right by θ, and the function

can be rewritten as

$$y = \text{sigmoid}(s - \theta) \tag{4.2.8}$$

The decisive analog model is shown in Fig. 4.2.4, and the output of a decisive analog model can be calculated using Eq. (4.2.9) and Eq. (4.2.10).

$$s = \sum_{n=1}^{N} w_n x_n \tag{4.2.9}$$

$$y = \text{sigmoid}(s - \theta) \tag{4.2.10}$$

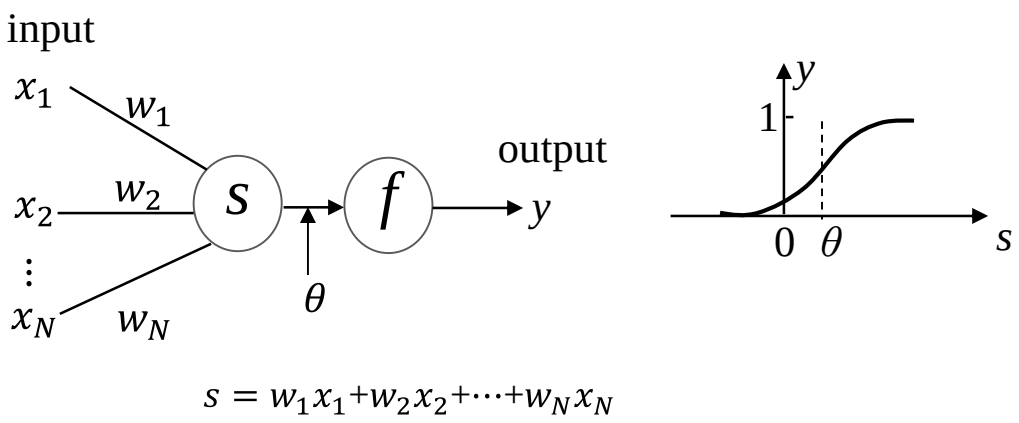

$$s = w_1x_1 + w_2x_2 + \cdots + w_Nx_N$$

Fig. 4.2.4. Decisive analog model.

As can be seen from Fig. 4.2.3, the decisive analog model has two kinds of parameters, the weights and the threshold. During the learning process, we modify the weights and thresholds to make the output of the network to approach our expected target output. Therefore, the fewer the number of parameters, the easier it is to modify. In order to unify the parameters for processing, we usually make some changes to the neurons as shown in Fig.4.2.5. It adds an input x_0, which takes a value of 1 to the input. Let the value of weight w_0 be -θ for this input. This means that the threshold θ can be treated as one of the weights. The

intracellular potential s and the output y of the neuron can be expressed by the following equation [83].

$$s = \sum_{n=0}^{N} w_n x_n \qquad (4.2.11)$$

$$y = f(s) \qquad (4.2.12)$$

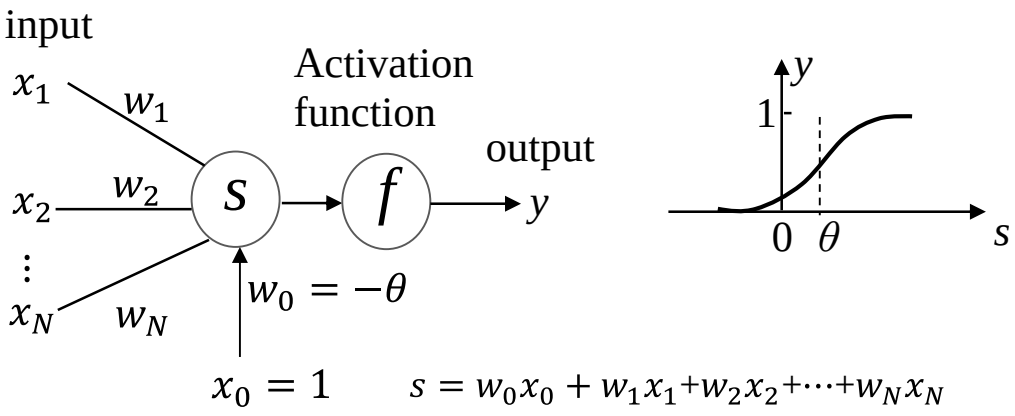

Fig. 4.2.5. Treat threshold as one of weights.

4.2.4 Architecture of Neural Network

As mentioned earlier, neural networks are constructed by interconnecting neurons that simulate human brain neurons. In practical applications, neural networks are generally divided into two categories. One is a feedforward neural network and the other is called a feedbackward neural network [81-83].

(1) Feedforward neural networks

The feedforward neural network consists of a series of layers, including an input layer, several hidden layers, and an output layer. The first layer, called the input layer, receives signals from the outside as input to the network. A simple schematic of a feedforward neural network is shown in Fig. 4.2.6.

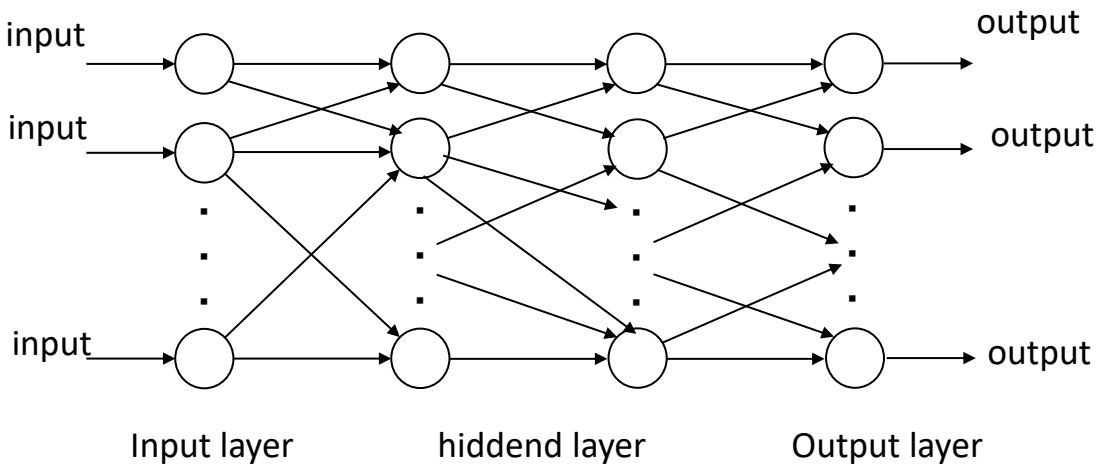

Fig. 4.2.6. An example of a feedforward neural network.

Each of the subsequent layers is connected to the previous layer, and the last layer produces the final output of the network. Inside the network, the signals propagate in the order of the input layer, the hidden layer, and the output layer, and are processed by the neurons at each layer, and the final operation result is outputted by the output layer. There is no signal feedback inside a feedforward neural network.

(2) Feedbackward neural networks

Unlike a feedforward neural network, within a feedback neural network, the signal flow is not unidirectional, but bidirectional. When determining the neurons on the input side, the values of the neurons on the output side must be considered at the same time. At the same time, the value of the neurons on the output side also depends on the value of the neurons on the input side. Figure 4.2.7 shows an example of a feedbackward neural network. We find that it is possible to exchange signals between arbitrary neurons. This makes the feedback neural network look very complicated.

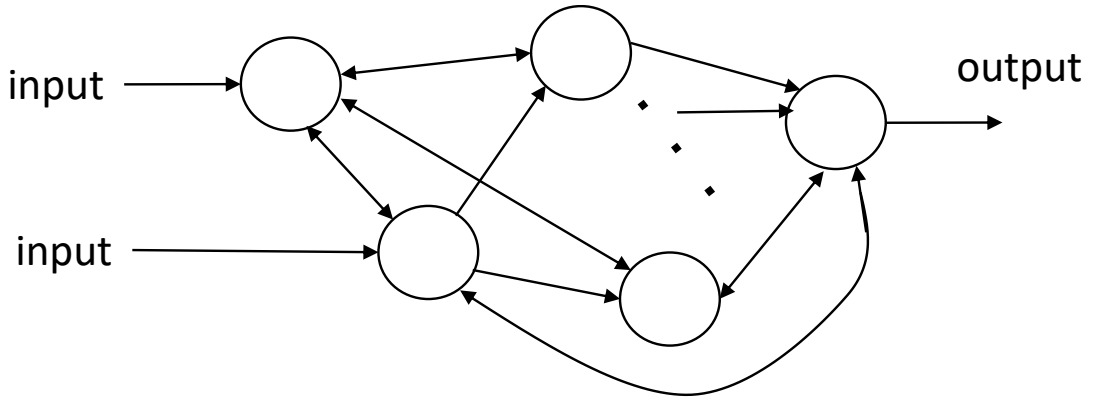

Fig. 4.2.7. An example of a recurrent neural network.

Since the signal is fed back from the output side to the neurons on the input side, the feedbackward type neural network has complex nonlinear dynamics and exhibits various time characteristics, which can be used to solve dynamic information processing [83].

4.3 Backpropagation Method

The error back propagation method is one of the learning methods of feedforward neural networks, and has been widely studied and actively used in neural network algorithms. The error back propagation method determines the parameters of the network based on the gradient method [82-85]. The error backpropagation network has three or more layers, but basically, it is usually three layers.

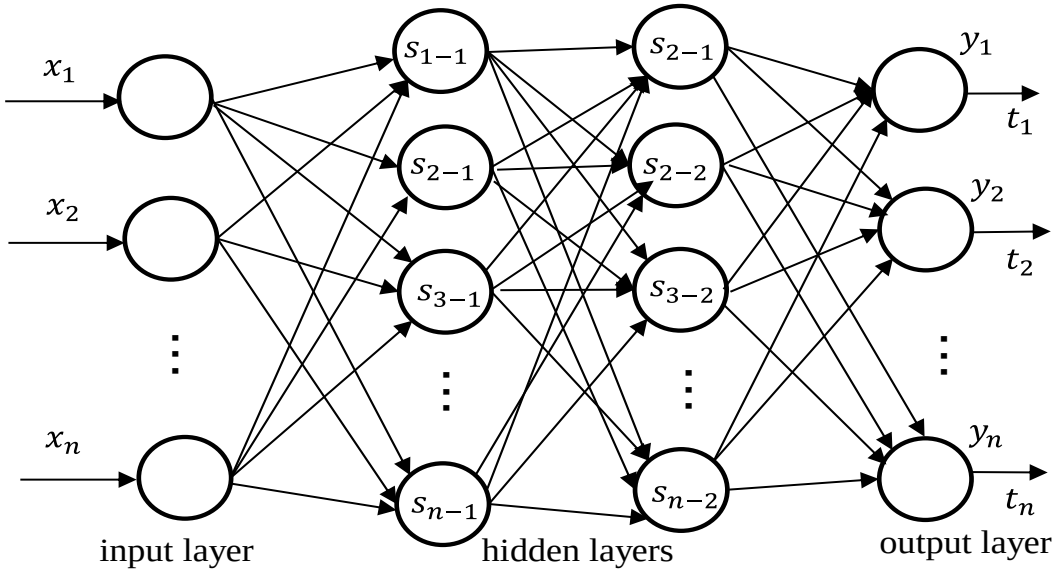

Fig. 4.3.1. Feedforward neural for error backpropagation method.

As shown in Fig. 4.3.1, there are known inputs ($x_1, x_2, \ldots\ x_N$) and corresponding target outputs ($t_1, t_2, \ldots\ t_N$). In the process of learning with neural networks, the neural network will give outputs ($y_1, y_2, \ldots\ y_N$). The purpose of our study is to make the error between the outputs ($y_1, y_2, \ldots\ y_N$) of the neural network and the target outputs ($t_1, t_2, \ldots\ t_N$) infinitely close to 0. We use the error evaluation function E to calculate the error between the outputs ($y_1, y_2, \ldots\ y_N$) and the target outputs ($t_1, t_2, \ldots\ t_N$), which is given as [83]

$$E = \sum_{n=1}^{N} |y_n - t_n|^2 \qquad (4.3.1)$$

In this study, the learning method we used was the backpropagation method. Change the relationship between inputs and outputs by changing the internal parameters (weights and thresholds) of the network.

Here, we take the feedforward neural network shown in Fig. 4.3.1 as an example. The neurons that make up the neural network are the neuron models we described in Section 4.2.3. In this case, the threshold is regarded as one of the weights, and only the weight of the neurons needs to be modified during the

learning process.

In this study, in order to process the experimental data, we used a three-layer feedforward neural network. Therefore, we are here to explain the error back propagation method based on the feedforward neural network. The measured values of the three parameters of the Stokes representing the polarization state are used as inputs, and the angle of rotation of the sensor is used as an output to the network. When designing neural networks, we must consider our actual data types and structures. For our experimental data, what we need is a three-input-one-output neural network, as shown in Fig. 4.3.2. Thus, we give the introduction of the error backpropagation method using the neural network shown in Fig. 4.3.2.

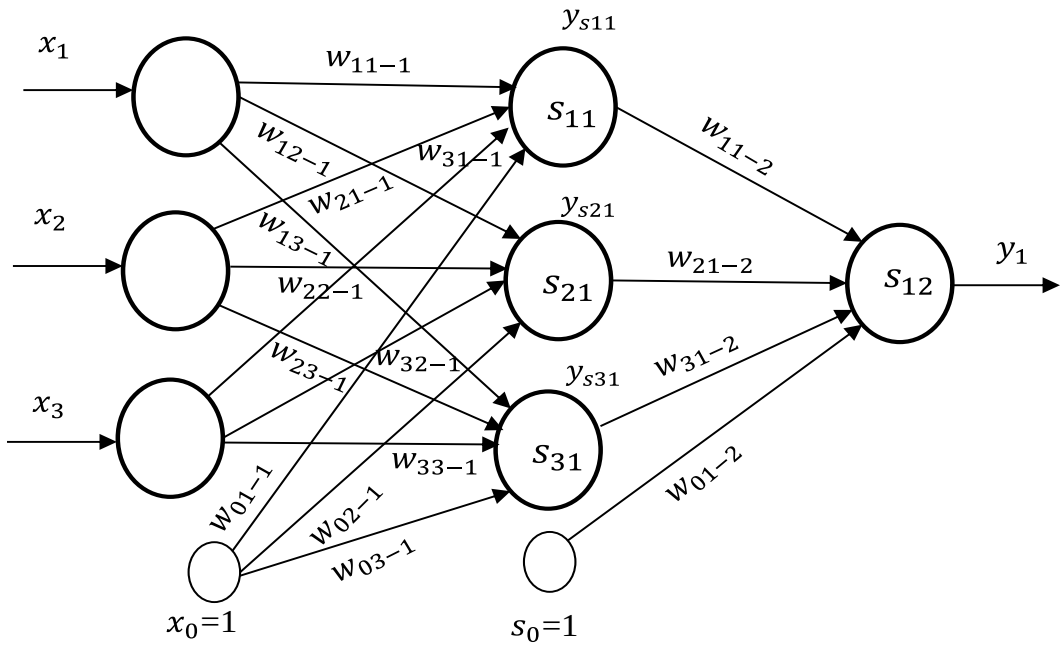

Fig.4.3.2. Forward mode of error backpropagation method.

In the learning process of the error back propagation method, it is divided into

two steps, one is the forward mode and the other is the backward mode. The step for calculating the actual output of the neural network in the order of the input layer to the output layer is called the forward mode, as shown in Fig.4.3.2. Here, the x_1 , x_2 and x_3 are inputs to the neural network, and the y_1 is the output of the neural network. The w represents the weight, and the threshold of each neuron is treated as a weight. So we add a neuron with an output of 1 and a threshold of $-\theta$ in each layers.

Before learning begins, we need to give each weight an initial value. The input and target output are then provided to the neural network and learning begins. Learning is actually to determine a set of weights that correctly represent the relationship between input and target output. When the learning is complete, the set of weights will be determined. The actual output of the neural network can be calculated according to the equations as follows:

$$S_{11} = w_{11-1}x_1 + w_{21-1}x_2 + w_{31-1}x_3 + w_{01-1}x_0 \quad (4.3.2)$$

$$y_{s11} = sigmoid(s_{11}) \quad (4.3.3)$$

$$y_1 = w_{11-2}y_{s11} + w_{21-2}y_{s21} + w_{31-2}y_{s31} + w_{01-2}s_0 \quad (4.3.4)$$

y_{s11} , y_{s21} and y_{s31} are the output of neurons in the hidden layer and are also the input to the output layer. In a neural network, the output of each layer is the input to the next layer connected to it. Therefore, we can determine the output of neurons of each layer in the order from the input layer to the output layer.

The next step is the backward mode that corrects the weights of each layer from the output layer to the input layer. The calculated difference $y_i - t_i$ between the actual outputs of the neural network and the target outputs is used as an input to the backward mode to modify the weight of the network. In

the backward mode, the signal propagates from the output layer to the input layer. The difference between the actual output of the neural network and the target output is given to the neural network shown in Fig.4.3.3, which are inputs to the backward mode. The y_{s11}, y_{s21} and y_{s31} are the outputs of neurons in the hidden layer calculated in the forward mode. The z represents the outputs of each neurons in the backward mode as shown in Fig. 4.3.4. And we can calculate it using Eq. (4.3.5).

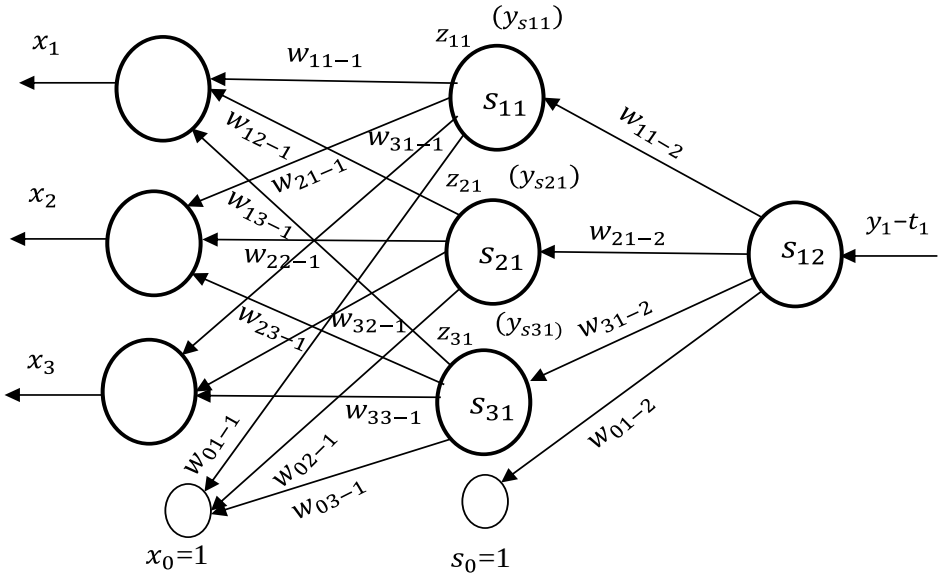

Fig. 4.3.3. Backward mode of error back propagation method.

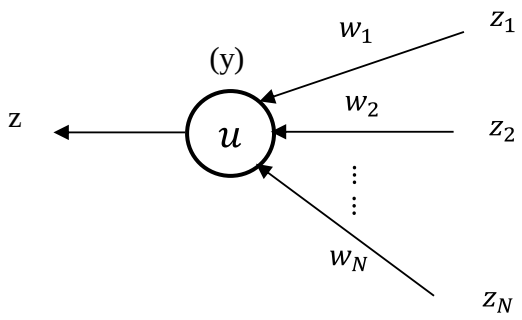

Fig. 4.3.4. Neuron model in backward mode.

$$z = sigmoid'(s)\sum_{n=1}^{N} w_n Z_n \qquad (4.3.5)$$

Here, the $\{Z_1, Z_2, \quad \cdots Z_N\}$ represent the inputs that are provided to the neuron, and $\{w_1, w_2, \quad \cdots w_N\}$ are the weights corresponding to the inputs. Then we use the derived function of the sigmoid function to calculate the outputs of neurons in backward mode. We use the calculated output z of each neuron to make minor modifications to the weights by Eq. (4.3.6).

$$w_{ij-(l+1)} = w_{ij-(l+1)} - \mu y_{sil} z_{j(l+1)} \qquad (4.3.6)$$

Here, μ is a small positive number that determines the amount of weight change in each learning process. The l represents the number of layers in which the neurons are located, and i and j represent the i-th neurons and the j-th neurons in the layer. The $w_{ij-(l+1)}$ represents the weight connecting the neuron of number i in layer l and the neuron of number j in layer$(l+1)$. Here we use a three-input-one-output feedforward neural network to explain the error backpropagation method. But in practice, we may encounter more complicated situations, and there may be dozens to hundreds of inputs. So we need to design the neural network according to the actual situation.

4.4 Design of Neural Network

The reason why neural networks are widely used is because of their learning ability, which is also considered to be its greatest feature. From the training data by using a learning method, we could get an approximate relationship that represents the relationship between the experimental data used as the training data. Then, use the obtained approximate relationship to give correct output for inputs other than training data. By optimizing the parameters of the neural network, a highly accurate approximation can be made [86-87]. In this research,

learning is performed using the above-mentioned error backpropagation method.

In this study, we decided to use a feedforward neural network consisting of an input layer, a hidden layer, and an output layer for data processing. In order to be able to get the output we expect, we must properly design the neural network according to our experimental data. Before designing a neural network, we need to determine the inputs and outputs that are provided to the neural network. Once the inputs and outputs are determined, the number of neurons in the input and output layers of the neural network is also determined. In the study, the rotation angle of the sensor is the value we require, so it is used as the output of the neural network. The measured values of the polarization state corresponding to the angle of rotation of the sensor are provided as an input to the neural network.

Since we are using a three-layer feedforward neural network, after the input layer and the output layer are determined, in order to obtain a satisfactory learning result, the appropriate number of neurons in the middle layer should be determined. If the number of neurons in the hidden layer is too small, although it may take a small amount of time to complete the study, it is often difficult to obtain satisfactory learning results. Conversely, if there are too many neurons in the hidden layer, not only will it take a lot of time to complete the study, but there may also be overfitting. In both cases, good learning outcomes are not guaranteed. In order to determine the appropriate number of neurons for the hidden layer and obtain satisfactory learning results, the Trial & Error method is used [31,82].

The steps of the Trial & Error method are as follows. First, we set up a small number of neurons for the hidden layer and start learning. If there is a large error in the learning result, we will increase the number of hidden layer neurons little

by little and observe the learning results. If the error becomes smaller, we then continue to increase the number of hidden layer neurons. If the error becomes larger, the number of hidden layer neurons should be reduced. Often this process has to go through many times until the error is not smaller any longer, and the number of neurons at this time is taken as the number of neurons in the hidden layer.

Similarly, the determination of the number of times of learning is equally important for achieving satisfactory learning outcomes. As with the method of determining the number of hidden layer neurons, we also adjust the number of learning times while observing the learning results. Similarly, the adjustment of the weight and the value of the gain during the learning process are also determined using the Trial & Error method. The gain is a parameter in the sigmoid function as described previously.

The learning procedure of the error backpropagation method could be expressed as Fig. 4.4.1 [88]. The learning process is consistent with our previous description. First, set the initial value for the parameters. The parameters include the number of neurons in the hidden layer, the number of learning times, the values of gain of the sigmoid function, the degree of weight correction and the initial value of weights. Then, the training data for determining the weights is provided, the inputs are $(x_0, x_1, \ldots\ x_L)$, and the outputs are $(y_0, y_1, \ldots\ y_L)$. After providing input to the neural network, the output of each neuron in each layer is calculated to obtain the actual output of the neural network. The program will then execute the backward mode to modify the weight value until the set number of learning times is completed.

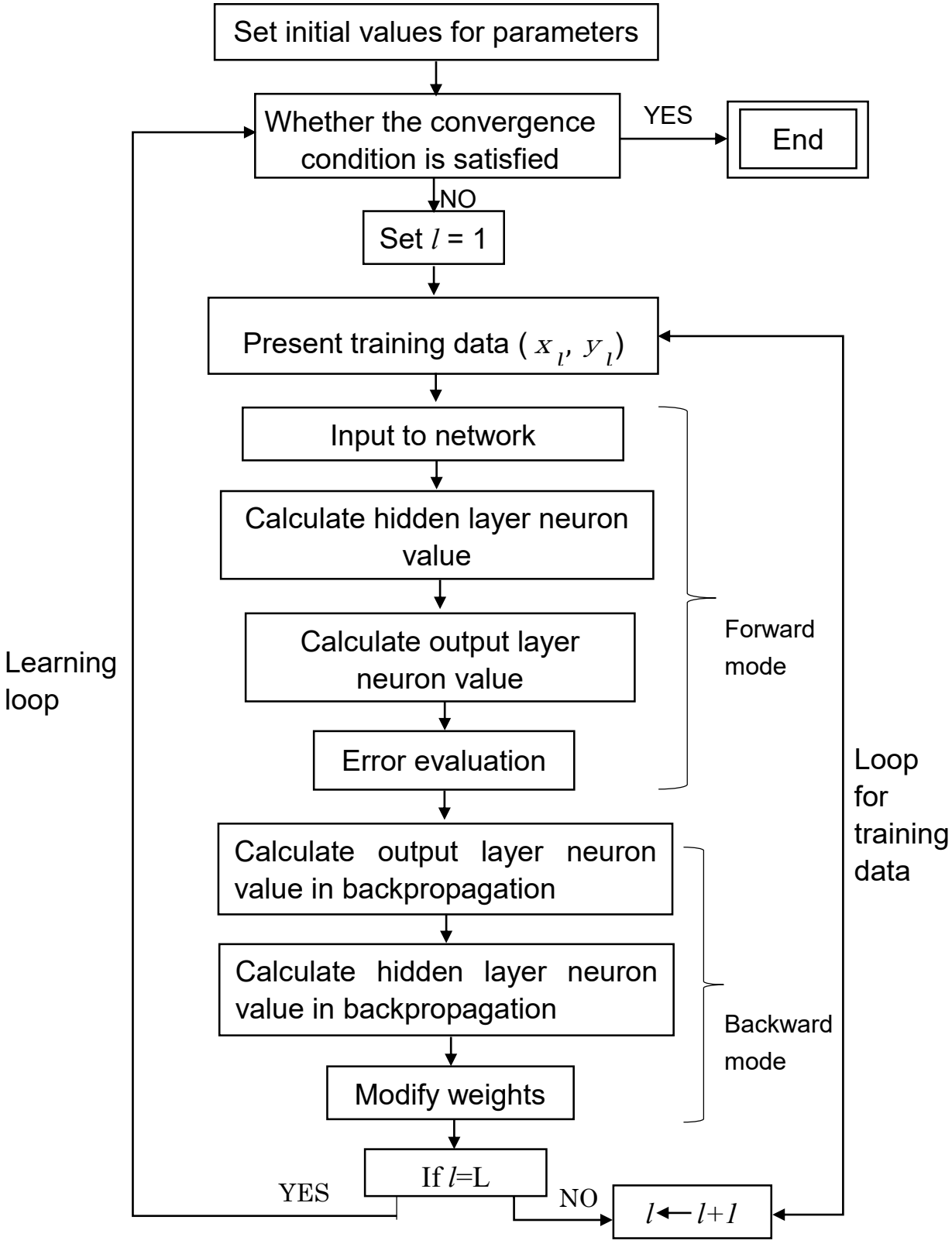

Fig.4.4.1. Learning procedure of the backpropagation method.

5. Experiments and Results

5.1 Verification of twisting when rotating the sensor

In this study, we use a common single-mode fiber that was wound into a circle shape as a sensor and the sensor is rotated by pulling the Invar wire attached to the sensor. The state of polarization is measured using a polarization analyzer. Since we do not know whether the twisting motion affects the experimental results when the sensor is rotated, it is necessary to detect whether the twisting motion of the rotated sensor affects the experiment before performing the strain experiment. If there is a twisting effect, then it must be taken into account. The experimental system for verification of twisting is shown in Figure 5.1.1 [32].

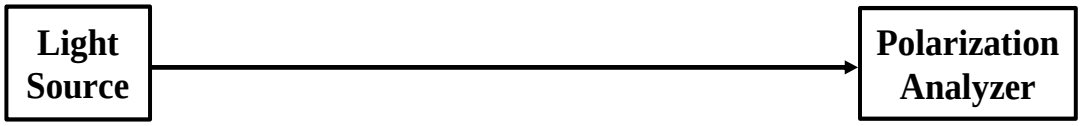

(a) Measurement of the light source.

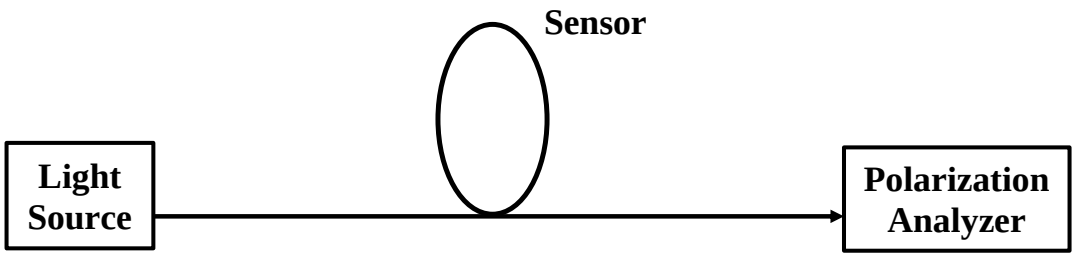

(b) Measurement of light transmitted through the sensor.

Fig. 5.1.1. Experimental systems for verifying twisting.

First, we connected the polarization analyzer directly to the light source to measure the state of polarization of the output light of the light source as shown in Fig 5.1.1.a. The next step is shown in Fig.5.1.1.b [32]. We used two 1-m-long fibers and wound them into a circle shape for use as the sensor. Then, we connected each fiber separately to the light source and conducted the experiment. In the experiment, we rotated the sensor from 0° to 180° at 10° intervals and

measured the polarization state of the transmitted light of the sensor. The two types of fibers used in the experiments were (a) an optical fiber without an outer jacket and (b) an optical fiber with an outer jacket, and the two types of fibers have different radii. When the fibers are wound into a circular shape as a sensor, their bending radii are 0.0215 m and 0.0205 m, respectively [32]. The phase difference of the sensor was calculated by Eq. 3.3.1 and Eq. 3.3.2. We used the measured state of polarization of the output light of the light source to calculate the state of polarization of the transmitted light from the rotated sensor. The calculation formula used is shown in Eq. 3.2.5. Then, we compared the calculated and measured values of the state of polarization of the transmitted light from the sensor, and their comparison is shown in Fig. 5.1.2. Here, S1, S2, and S3 denote the Stokes parameters that represent the state of polarization, which can be directly measured by the polarization analyzer in the experiment.

If the twisting motion does not affect the experimental results when the sensor is rotated, the measured values of the state of polarization of the transmitted light from the sensor should be the same as the calculated values. However, as shown in Fig. 5.1.2, their values do not match with each other no matter which type of optical fiber is used [32]. This means that the twisting motion has influences on experiment results when the sensor is rotated. Then, we must also take this twisting effect into account for calculation when the strain experiment is performed.

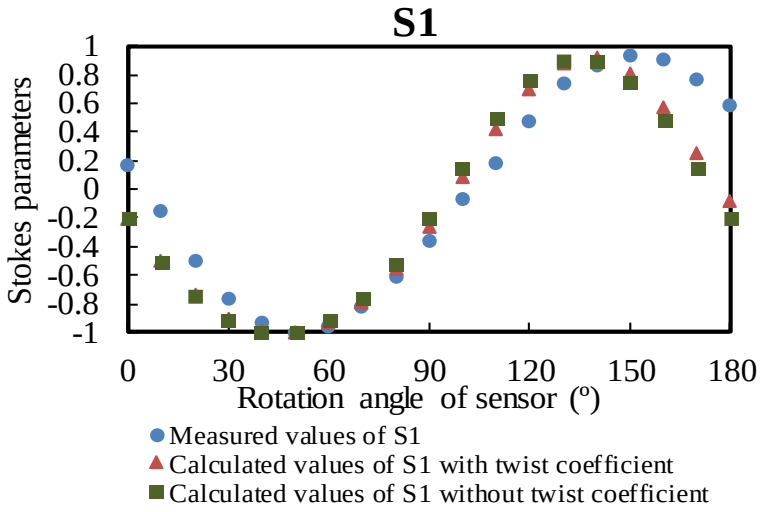

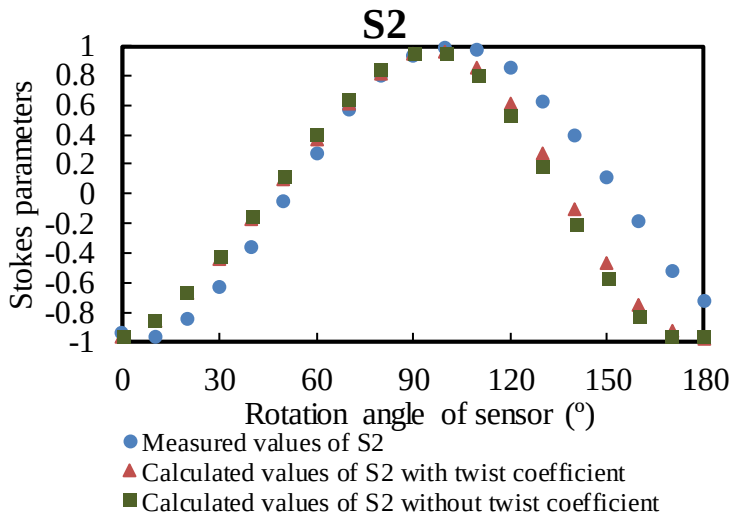

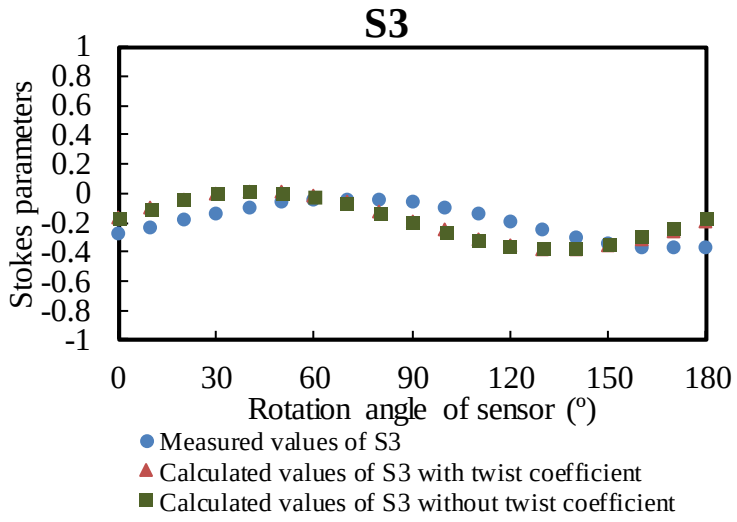

(a) Results using fibers without an outer jacket.

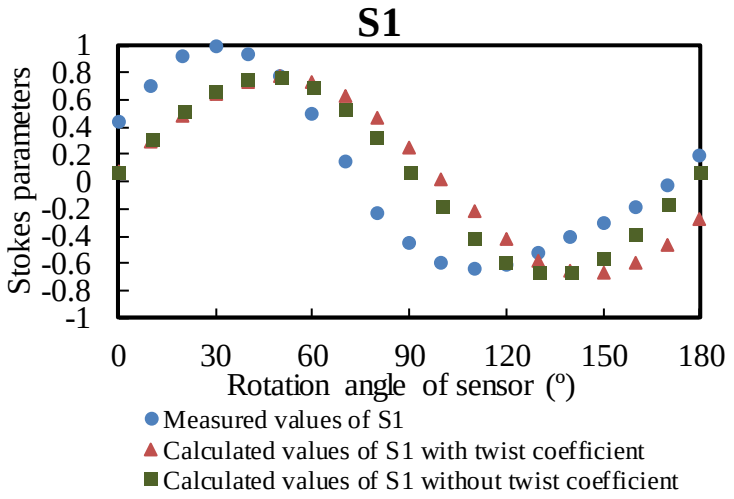

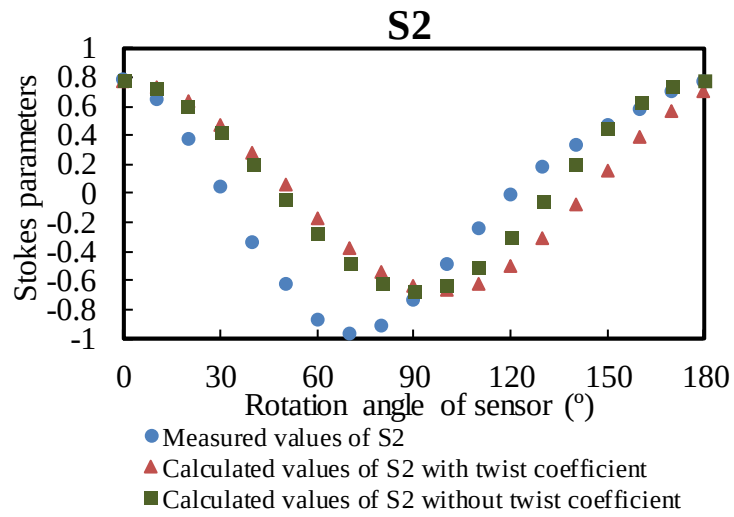

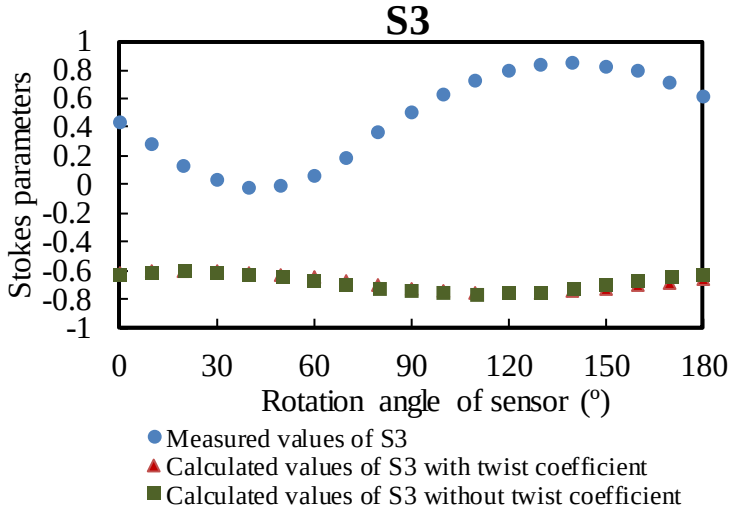

(b) Results using fibers with an outer jacket.

Fig. 5.1.2. Experiment for verifying twisting.

Furthermore, according to previous research, when the optical fibers are rotated, twisting occurs and the corresponding constant is known as the twisting coefficient [78]. Then, the state of polarization of the transmitted light from the sensor was calculated from the measured values of the state of polarization of the light source using Eq. 3.2.5 with twisting coefficient [32]. The results calculated with consideration of this twisting coefficient are shown in Fig. 5.1.2 [32]. If this twisting coefficient can represent the twisting effect generated by the rotation of the optical fiber, the results calculated using this twisting coefficient should be consistent with the measured results shown in Fig. 5.1.2. However, the calculated values of the state of polarization of the transmitted light from the sensor and the measured values of the state of polarization of the transmitted light from the sensor still did not match. This means that we can neither ignore the twisting effect caused by the rotation of the optical fiber nor simply use the twisting coefficient to calculate the twisting. Therefore, due to the occurrence of the twisting and its effect on the state of polarization, we believe that it is possible to calculate the twisting as a rotated wave plate. The feasibility is also verified by the following experimental results.

5.2 Experiment using Jones calculus and Results

5.2.1 Experiment system

The strain measurement experimental system used in this study is shown in Fig. 5.2.1 [32]. We used an LD light source and a polarization analyzer to measure changes in the state of polarization of light propagating within the optical fiber as the sensor rotates. In the experiment, there is an invar line connected to the sensor, and we pulled the Invar line to rotate the sensor.

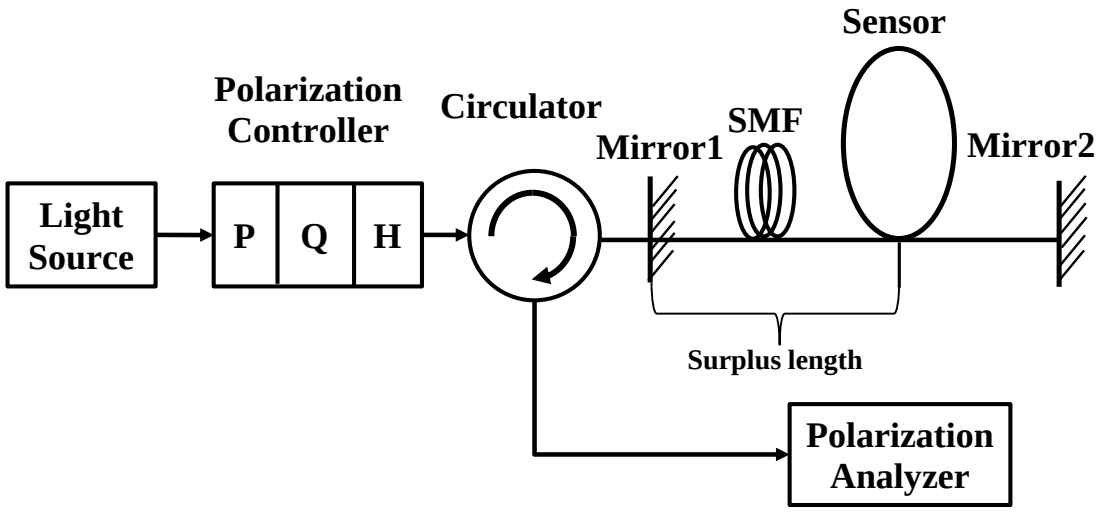

Fig. 5.2.1. Schematic diagram of the experimental system.

The pulsed light from the light source passes through the polarization controller and entered the sensor via the optical circulator. The Fresnel reflected light that was generated by the reflecting mirrors was incident on the polarization analyzer through the optical circulator. As can be seen from Fig. 5.2.1, there are two reflecting mirrors in the experimental system, the reflecting Mirror 1 and the reflecting Mirror 2. Their reflected light is measured by the polarization analyzer. As long as the state of polarization of the output light of the light source does not change, the polarization state of the reflected light of the Mirror 1 will not change. And, the polarization state of the incident light entering the sensor is calculated using the polarization state of the reflected light of Mirror 1. On the other hand, the reflected light from the Mirror 2 is affected by the rotation of the sensor. That is, the polarization state of the reflected light of the Mirror 2 changes as the sensor rotates. In the experiment, since the polarization state of the reflected light of the Mirror 2 changes with the rotation of the sensor, we use the measured polarization state to calculate the rotation angle of the sensor. And then using the

rotation angle of the sensor to calculate the displacement of the Invar line and the strains applied in the experiment. In the experiment, we used pulsed light to perform the measurement, so that when the pulsed light output from the light source is reflected by the Mirror 1 and Mirror 2, there will be a time delay between the two reflected light from Mirror 1 and Mirror 2. We used a 600-m- long optical fiber to prevent the overlap of the two reflected pulses. The wavelength of the light source was 1550 nm, the repetition frequency was 1 kHz, the pulse width of the incident light was set to 3 μs. The maximum sampling frequency of the polarization analyzer was 1,046 kHz. In this study, we used the polarization state calculated by the Jones matrix instead of the measured polarization state to calculate the rotation angle of the sensor. The calculation results given in the following sections also demonstrated the feasibility of the proposed calculation method.

5.2.2 Experiment and results

In the previous chapter, we described that we propose to use the Jones matrices of two rotated wave plates to calculate an arbitrary optical path. In order to get the correct calculation results, we must determine the Jones matrices of the two rotated wave plates representing each optical path. Therefore, before performing the strain measurement experiment, we must conduct experiments to determine the Jones matrices for each optical path, including the optical circulator part and the surplus length part. When the sensor is rotated, we can use the obtained Jones matrices representing the optical path to calculate the state of polarization of the transmitted light from the sensor. This means that we could get the polarization state of the incident light entering the second sensor during multi-

point measurement using the calculus. Then, we measured the polarization state of the reflected light of the Mirror 1 and Mirror 2 when the sensor is rotated. The rotation angle of the sensor was obtained from the polarization state of the reflected light from Mirror 1 and Mirror 2, and then the strains applied in the experiment were determined.

5.2.2.1 Determination of the Jones matrices for the optical circulator.

We use the experimental systems shown in Fig. 5.2.2 to obtain the Jones matrices of the two rotated wave plates representing the optical circulator section [32]. Here, we assume that the two Jones matrices representing the optical circulator section are $\mathbf{J_1}$ and $\mathbf{J_2}$, respectively [32]. The polarization state of transmitted light and the polarization state of the reflected light from the optical circulator were measured separately.

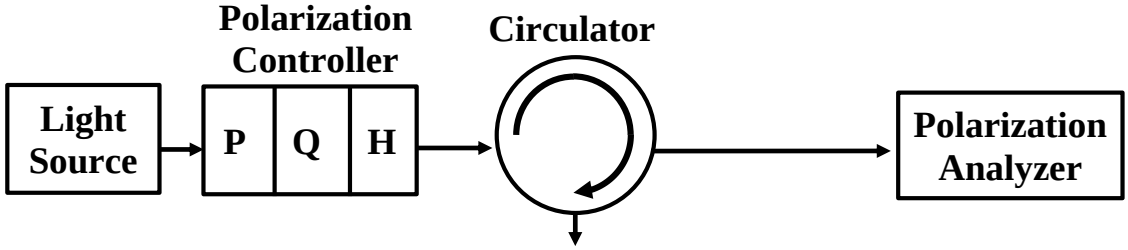

(a) Measurement of transmitted light from the optical circulator.

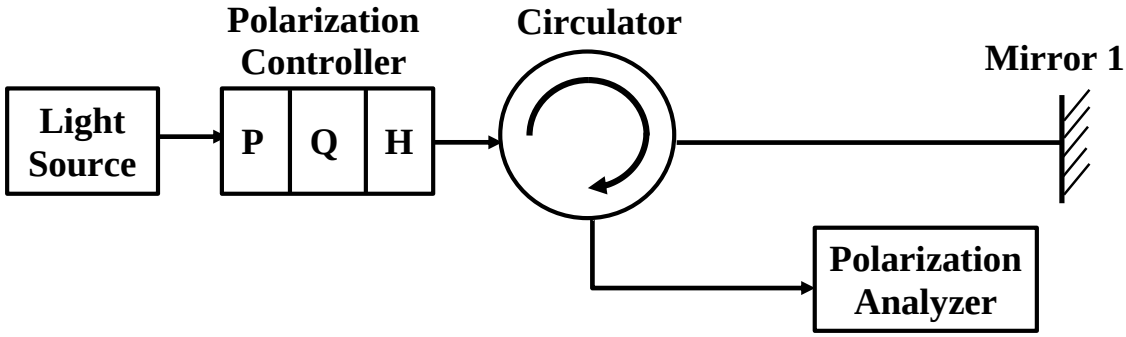

(b) Measurement of reflected light from the optical circulator.

Fig. 5.2.2. The experiment of the optical circulator.

The Jones matrices representing the optical circulator were obtained through

this measurement. In the experiment, first, the linear polarizer (P) of the polarization controller was set to 0°, and the quarter-wave plate (Q) of the polarization controller was set to 45°. Then, we measured the polarization state of the transmitted light and the reflected light from the optical circulator by rotating the half wave plate (H) from 0° to 90° at 10° intervals. Then, we measured the polarization state of the transmitted and reflected light from the optical circulator again by rotating the half-wave plate (H) from 0° to 90° at 10° intervals when the linear polarizer (P) is set to 0° the quarter-wave plate (Q) is set to 90°.

Initially, $\mathbf{J_1}$ and $\mathbf{J_2}$ can be expressed as the inverse matrices of the Jones matrices as shown in Eq. (3.2.8) [32]. That is because we use Eq. (3.2.8) to calculate the polarization state of the reflected light from Mirror 1 using the polarization state of the transmitted light of the optical circulator. Here, the reflected light from Mirror 1 means the reflected light from the optical circulator. We obtained the parameters of $\mathbf{J_1}$ (θ_1, ϕ_1) and $\mathbf{J_2}$ (θ_2, ϕ_2). The equation for calculating the polarization state of transmitted light from the optical circulator using the measured polarization state of the reflected light is expressed as [32]:

$$\begin{bmatrix} \text{transmitted light} \\ \text{from circulator} \end{bmatrix} = \mathbf{J}_2 \cdot \mathbf{J}_1 \cdot \begin{bmatrix} \text{reflected light} \\ \text{from Mirror 1} \end{bmatrix}. \qquad (5.2.1)$$

Then, we calculated the polarization state of the transmitted light through changing the orientation angles (θ_1, θ_2) and phase differences (ϕ_1, ϕ_2) of $\mathbf{J_1}$ (θ_1, ϕ_1) and $\mathbf{J_2}$ (θ_2, ϕ_2) from 0º to 180º at 1º intervals. Then we compared the calculated and measured values of the state of polarization of the transmitted

light to determine the parameter values that minimize the error between them.

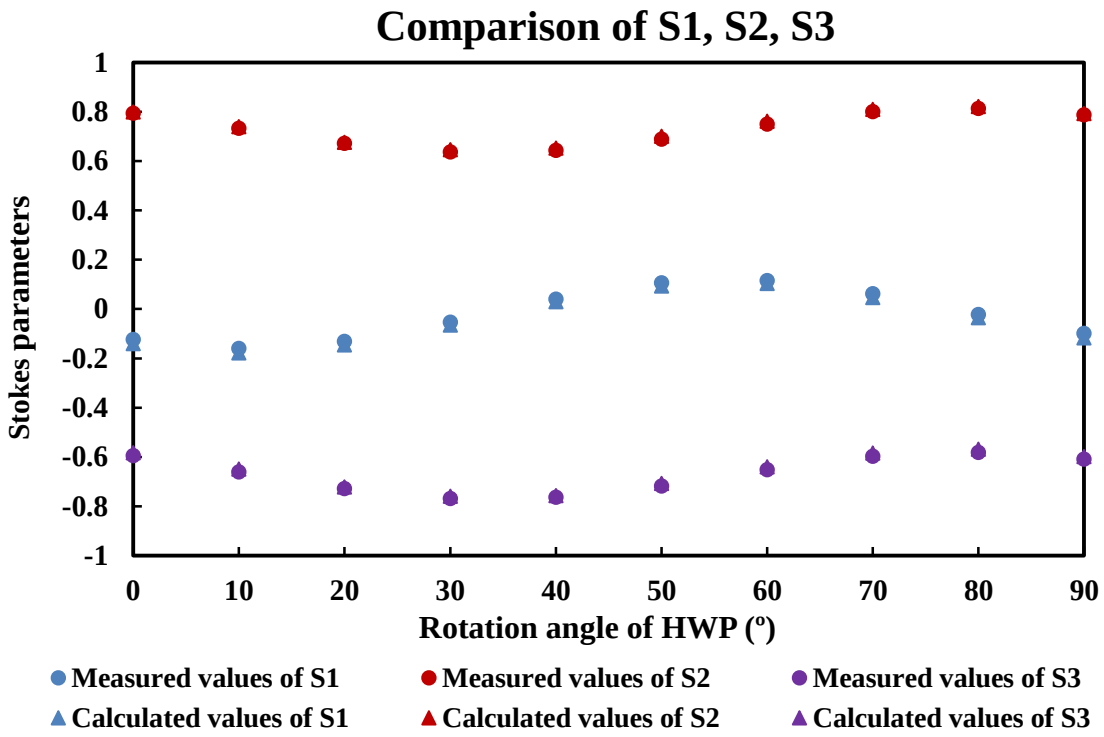

Fig.5.2.3. Comparison of the measured values and the calculated values of the transmitted light from the optical circulator when the quarter-wave plate is at 45º.

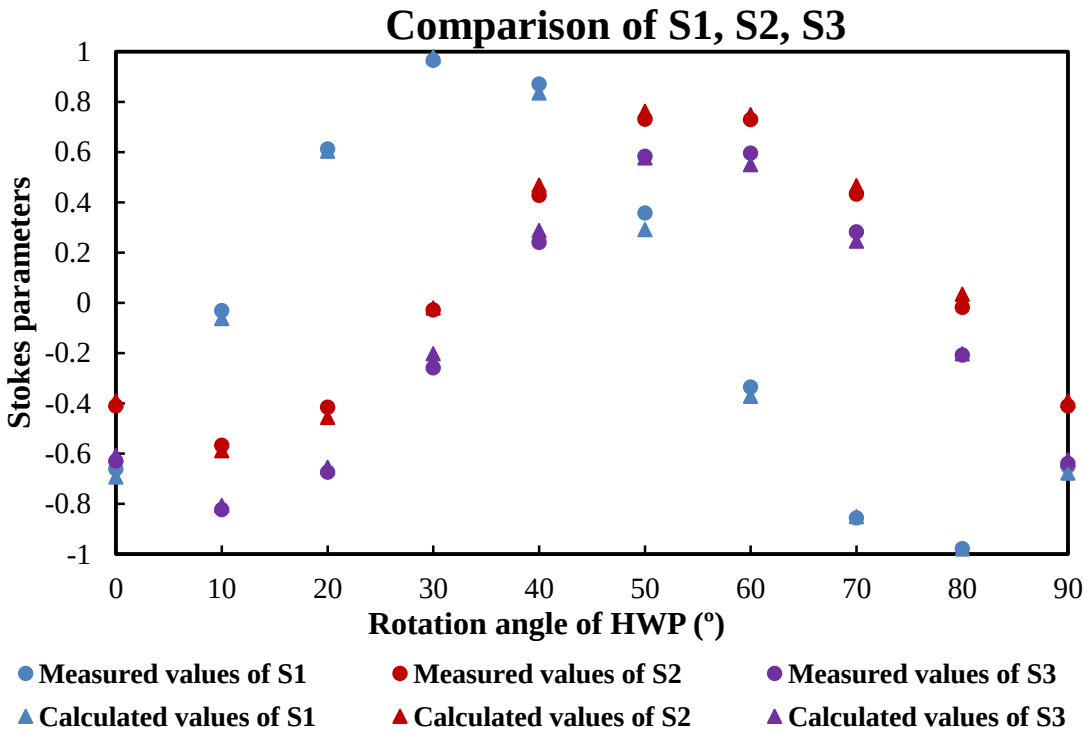

Fig.5.2.4. Comparison of the measured values and the calculated values of the transmitted light from the optical circulator when the quarter-wave plate is at 90°.

Table 5.2.1 Calculated parameters for the optical circulator.

	Orientation angle (°)	Phase difference (°)
$\mathbf{J_1}$ (θ_1, ϕ_1)	θ_1 = 1	ϕ_1 = 150
$\mathbf{J_2}$ (θ_2, ϕ_2)	θ_2 = 38	ϕ_2 = 106

The comparison between the calculated values of the polarization state of the transmitted light and the measured polarization state of the transmitted light is shown in Fig. 5.2.3 and Fig. 5.2.4 when the quarter-wave plate is at 45° and 90°, respectively [32]. Table 5.2.1 lists each of the parameters we obtained [32]. Furthermore, from Fig. 5.2.3 and Fig. 5.2.4, we find that the calculated and measured values of the polarization state of the transmitted light of the optical

circulator are in good agreement with each other. Therefore, by substituting the measured values of the polarization state of the reflected light from the optical circulator and the matrices $\mathbf{J_1}$ (θ_1, ϕ_1) and $\mathbf{J_2}$ (θ_2, ϕ_2) obtained above into Eq. (5.2.1), we can calculate the polarization state of the transmitted light from the optical circulator. In order to ensure that no interference affects the optical path during the experiment, we set P, Q, and H to 0°, and measured the polarization state before and after the experiment. Since the two sets of measurement data were consistent with each other, it is proved that no interference affects the optical path.

5.2.2.2 Determination of the Jones matrices for the surplus length.

The surplus length is a length of single-mode fiber connecting the Mirror 1 and the sensor, as shown in Fig. 5.2.1. Here we used the polarization state of the transmitted light from the Mirror 1 measured in 5.2.2.1. We assume that the Jones matrices representing the surplus length are $\mathbf{J_3}$ and $\mathbf{J_4}$. The state of polarization of the light that was transmitted through the sensor (without rotating the sensor) was measured using the experimental system illustrated in Fig. 5.2.5 [32].

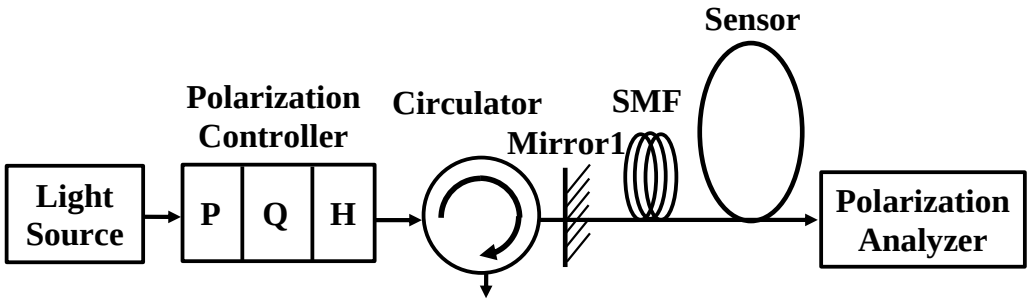

Fig. 5.2.5. Measurement of the transmitted light from the sensor.

In the experiment, we set the polarization controller's linear polarizer (P) to 0º and the quarter-wave plate (Q) to 45º. Then, we measured the polarization state of the transmitted light from the sensor at 10º intervals when rotating the half-

wave plate (H) from 0º to 90º. Then the Q was set to 90º, and we measured the polarization state of the transmitted light from the sensor at 10º intervals when rotating the half-wave plate (H) from 0º to 90º. As described previously, $\mathbf{J_3}$ and $\mathbf{J_4}$ are the two rotated wave plates that represent the surplus length, and we can express them using the Eq. (3.2.8). The parameters of $\mathbf{J_3}$ (θ_3, ϕ_3) and $\mathbf{J_4}$ (θ_4, ϕ_4) were determined. Furthermore, we can also express the sensor after $\mathbf{J_4}$ as a rotated wave plate. We set the orientation angle of the sensor to 0° and the phase difference to 34.43° to determine the Jones matrices of the surplus length part. And, the phase difference used here was obtained in Sect. 3.3. Then, we used the polarization state of the transmitted light from the optical circulator to determine the polarization state of the transmitted light from the sensor. The equation we used to perform this calculation is expressed as follows [32]:

$$\begin{bmatrix} \text{transmitted light} \\ \text{from sensor} \end{bmatrix} = [\text{sensor}] \cdot \mathbf{J}_4 \cdot \mathbf{J}_3 \cdot \begin{bmatrix} \text{transmitted light} \\ \text{from circulator} \end{bmatrix} \qquad (5.2.2)$$

Then, by changing the orientation angles (θ_3, θ_4) and phase differences (ϕ_3, ϕ_4) of $\mathbf{J_3}$ (θ_3, ϕ_3) and $\mathbf{J_4}$ (θ_4, ϕ_4) from 0º to 180º at 1º intervals, we calculated the polarization state of the transmitted light from the sensor. In order to find the parameter values that minimize the difference between them, we compared the calculated values and measured values of the polarization state of the transmitted light from the sensor.

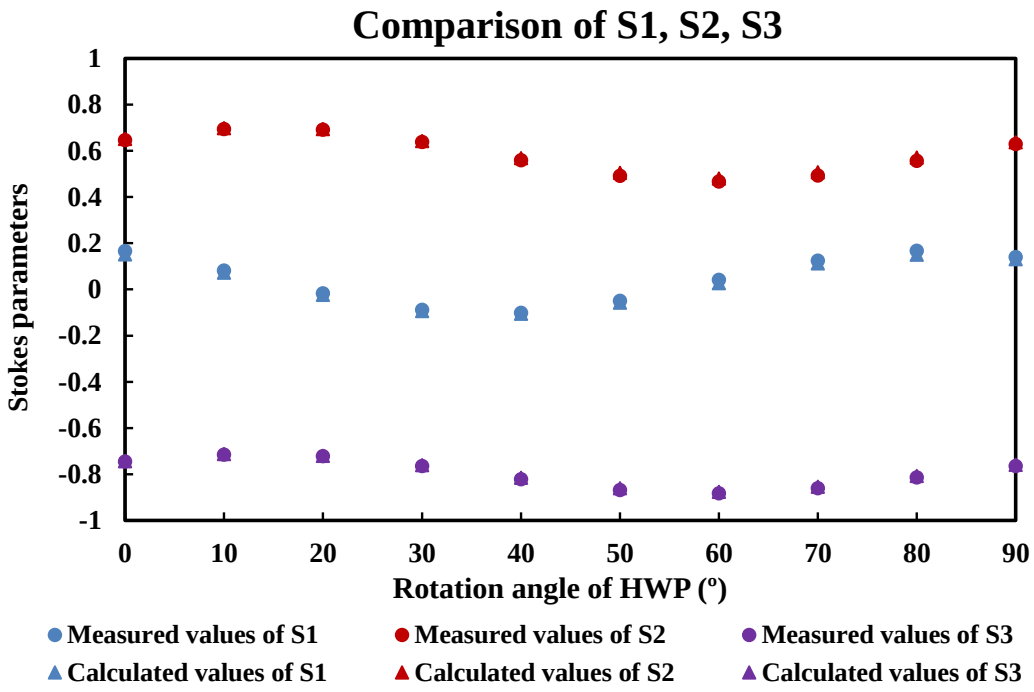

Fig. 5.2.6. Comparison of the measured values and the calculated values of the transmitted light from the sensor when the quarter-wave plate is at 45º.

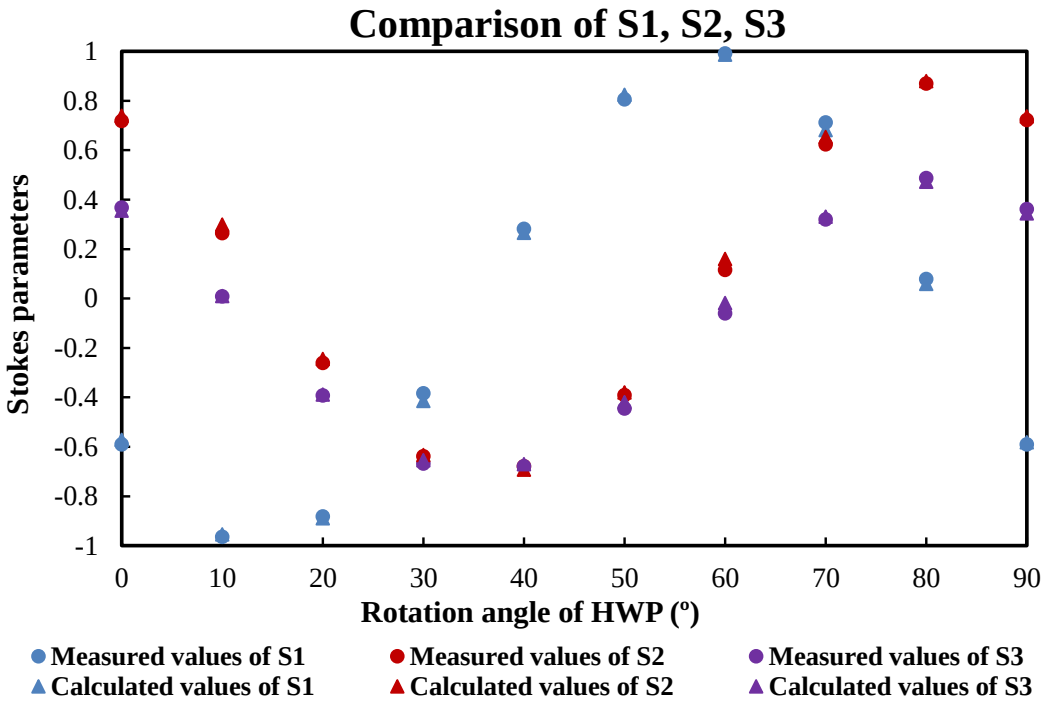

Fig. 5.2.7. Comparison of the measured values and the calculated values of the transmitted light from the sensor when the quarter-wave plate is at 90º.

Figure 5.2.6 and Figure 5.2.7 show the comparison between the calculated polarization state of the transmitted light and the measured polarization state of the transmitted light form the sensor when the quarter-wave plate is at 45º and 90º, respectively [32]. Table 5.2.2 lists each parameter that we obtained [32]. It can be seen from Fig. 5.2.6 and Fig. 5.2.7 that the calculated and measured values of the polarization state of the transmitted light from the sensor are very consistent with each other whether Q is 45º or 90º. This also shows that we correctly obtained the Jones matrices representing the surplus length part.

Table 5.2.2 Calculated parameters for the surplus length.

	Orientation angle (º)	Phase difference (º)
J3 (θ_3, ϕ_3)	θ_3 = 25	ϕ_3 = 124
J4 (θ_4, ϕ_4)	θ_4 = 85	ϕ_4 = 139

In order to ensure that no disturbance affects the optical path during the experiment, we set P, Q, and H to 0°, and measured the polarization state before and after the experiment. The two sets of measurement data were consistent with each other, demonstrating that no interference affected the optical path.

5.2.3 Changes in the polarization state due to the rotation of the sensor.

Here, we used the Jones matrices representing the optical circulator and the surplus length that were obtained in the previous sections to calculate the polarization state of the transmitted light from the sensor. The measured values of the polarization state of the reflected light from Mirror 1 used here are those that were measured in Sect. 5.2.2.1 when P, Q, and H were all set to 0º. We measured the polarization state of the transmitted light from the sensor using the experimental system shown in Fig. 5.2.5. In the experiment, we set P, Q, and H to 0° and rotated the sensor from 0° to 180° at 10° intervals. It has been

demonstrated in Section 5.1 that twisting occurs when the sensor rotated. Therefore, when calculating the polarization state of the transmitted light from the sensor, we must add a matrix representing the twisting to the calculation equation. The matrix of the twisting is expressed by Eq. (3.2.8). Thus, the equation for calculating the state of polarization of the transmitted light from the sensor is expressed as [32]:

$$\begin{bmatrix}\text{transmitted light}\\ \text{from sensor}\end{bmatrix} = [\text{sensor}][\text{twisting}] \cdot \mathbf{J}_4 \cdot \mathbf{J}_3 \cdot \mathbf{J}_2 \cdot \mathbf{J}_1 \cdot \begin{bmatrix}\text{reflected light}\\ \text{from Mirror 1}\end{bmatrix} \quad (5.2.3)$$

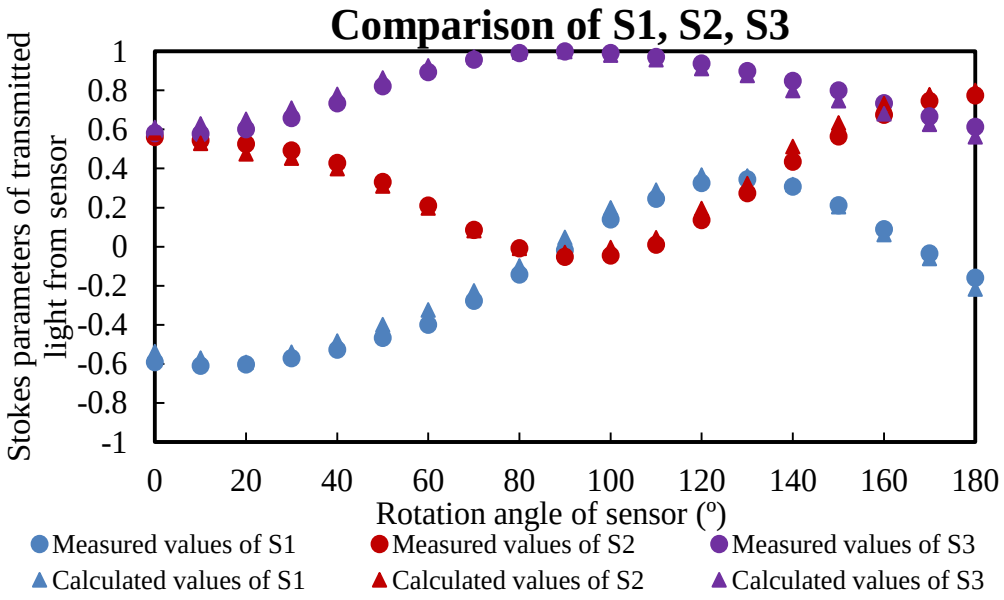

Fig. 5.2.8. Comparison of the measured values and the calculated values of the transmitted light from the rotated sensor.

The comparison of the measured values and calculated values of the polarization state of the transmitted light from the rotated sensor is shown in Fig. 5.2.8 [32]. The calculated values used here were obtained using Eq. (5.2.3). As can be seen from Fig. 5.2.8, the calculated values of the polarization state of the transmitted light from the rotated sensor are in good agreement with the

measured values. Therefore, we can use the calculated values to replace the measured values of the polarization state of the transmitted light of the rotated sensor in the experiment. Thus, even if another sensor is connected in series from the back, the polarization state of the light into the second sensor can be accurately determined. In this way, it is thought that the influence of the front-end sensor on the rear-end sensor can be solved in the multi-point strain measurement experiment.

Then, we performed a strain measurement experiment with a single sensor using the experimental system shown in Fig. 5.2.1. In the experiment, we measured the polarization state of the reflected light from Mirror 1 and Mirror 2 when the sensor was rotated. As the sensor rotates, the change in the polarization state of the reflected light from the sensor is shown in Fig. 5.2.9 [32]. Here, the reflected light of the sensor means the reflected light from Mirror 2.

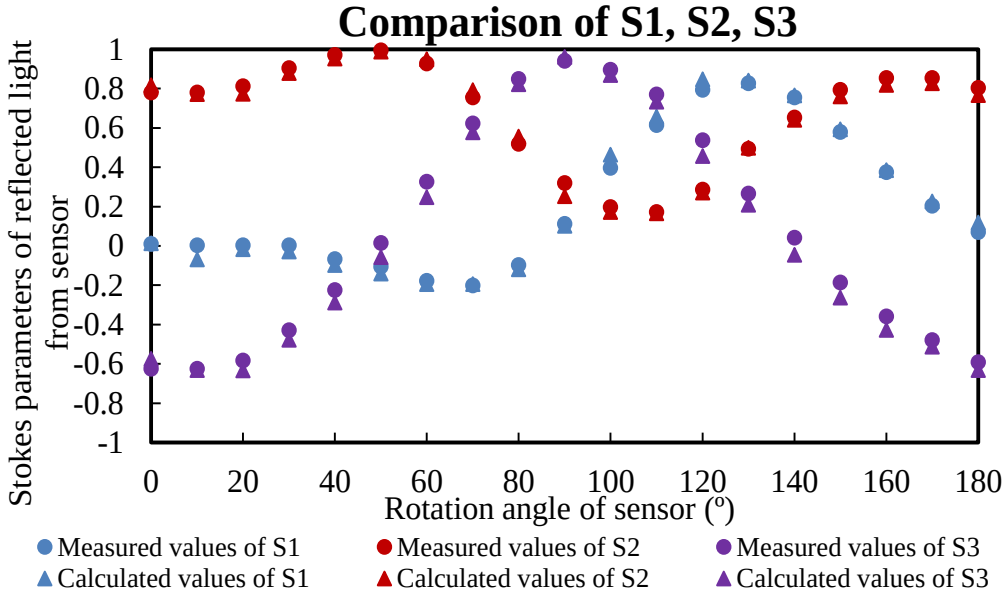

Fig. 5.2.9. The relationship between the polarization state of the reflected light and the rotation angles of the sensor.

As can be seen from Fig. 5.2.9, when the sensor rotates, the calculated values of the polarization state of the reflected light from the sensor agrees well with the measured values as the sensor rotates. This calculated value was obtained using the measured values of the polarization state of the reflected light from Mirror 1 as described above. Then, a function fitting was performed using the calculated values shown in Fig. 5.2.9 instead of the measured values. Through function fitting, we obtained three sets of approximate expressions for the Stokes parameters expressed by the rotation angle of the sensor. Then we run the C program to change the rotation angle of the sensor from 0° to 180° at 1° interval, and obtained 181 sets of Stokes parameters [32]. Then, we compared the measured values of the polarization state of the reflected light from the sensor with the 181 sets of Stokes parameters to obtain the rotation angle when the error is minimal. The comparison between the angle obtained in the program and the rotation angle applied in the experiment is shown in Fig. 5.2.10 [32].

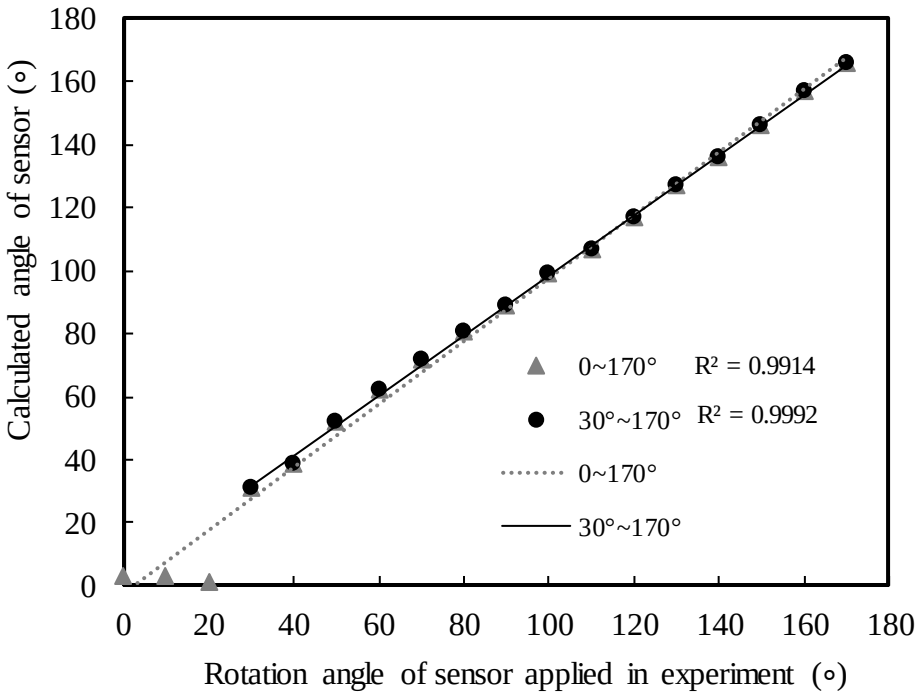

Fig. 5.2.10. Comparison of the calculated angles with the angles that were applied in the experiment.

We performed linear approximation separately at intervals of 0º~170º and 30º~170º and obtained the values of R^2, which are 0.9914 and 0.9992, respectively. The value of R^2 is larger in 30º~170º; therefore, the accuracy in this interval is higher. Hence, this interval was determined to be the measurement range. The reason why the error occurs in the interval of 0°~30° is that the change in the polarization state is very small in the interval from 0°~30° as shown in Fig.5.2.9. It is believed that the overall error may be reduced in the range of 0°~180° by varying the incident light. Then the strains applied in the experiment were obtained from rotation angles using a simple mathematical calculation using Eq. (3.3.3) and (3.3.4). The comparison between the calculated strains and the strains applied in the experiment is shown in Fig. 5.2.11 [32].

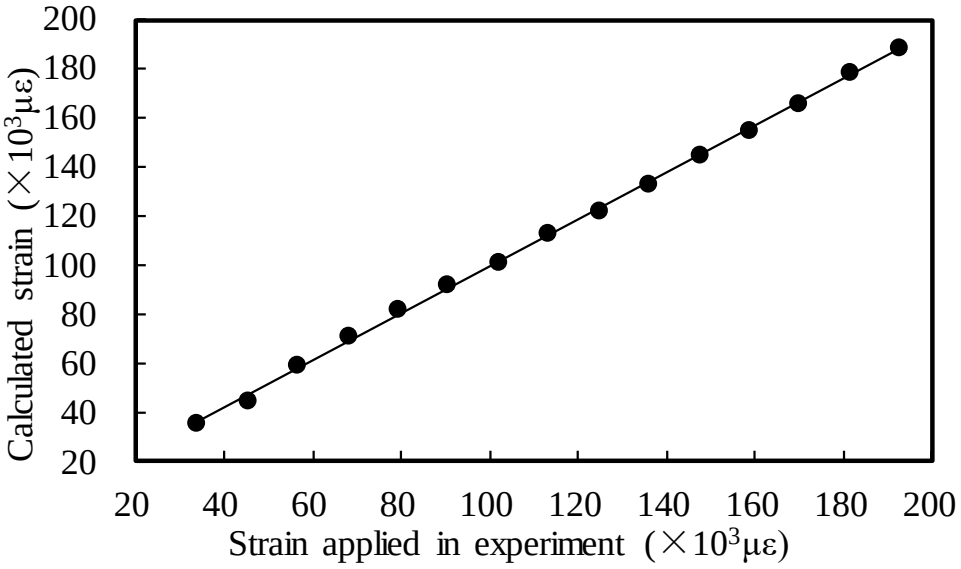

Fig.5.2.11. Comparison of the calculated strains with the strains that were applied in the experiment.

As can be seen from Fig. 5.2.11, there is an excellent linear relationship between the calculated strains and the strains applied in the experiment. Table 5.2.3 shows the relationship between the strains applied in the experiment and the calculated strains [32]. We found that the relative errors between them are within 4%. This demonstrates the feasibility of the proposed polarization strain sensor system using the Jones matrices of two rotated wave plates to calculate an arbitrary optical path. In addition, we performed the quantification of the strain measurement range with high accuracy by comparing the calculated strains with the strains applied in the experiment. Here, the strain measurement range was quantified by using the calculated values of the polarization state of the reflected light from the sensor. Therefore, in the strain measurement experiment, we can use the calculated values to effectively replace the measured values and obtain high-precision results. In addition, when multiple sensors are connected in series

for multi-point strain measurement, measuring the polarization state of reflected light from each sensor is very time-consuming. This replacement not only saves a lot of time and labor but also improves the operability of the measurement system.

Table 5.2.3 Relative errors between the applied and calculated strains.

Rotation angle of sensor (º)	Strain applied in the experiment ($\times 10^3 \mu\varepsilon$)	Calculated strain ($\times 10^3 \mu\varepsilon$)	Relative error (%)
30	34.03	35.17	3.3
40	45.38	44.24	2.5
50	56.72	58.99	4.0
60	68.07	69.20	1.7
70	79.41	79.41	0.0
80	90.76	91.89	1.3
90	102.10	100.97	1.1
100	113.45	112.31	1.0
110	124.79	121.39	2.7
120	136.14	132.73	2.5
130	147.48	144.08	2.3
140	158.83	154.29	2.9
150	170.17	165.63	2.7
160	181.51	178.11	1.9
170	192.86	188.32	2.4

5.3 Experiment using a Neural Network and Results

In the experiment, we rotated the sensor by pulling the invar wire connected to the sensor from 0 to 180º at 10º intervals, while the linear polarizer (P), the quarter-wave plate (Q), and the half-wave plate (H) were all set to 0º. The changes in the polarization states of the reflected light from the sensor with the rotation angle of the sensor are shown in Fig. 5.3.1. As described previously, the

Stokes parameters S1, S2, and S3 represent the polarization states, which can be directly measured by the polarization analyzer.

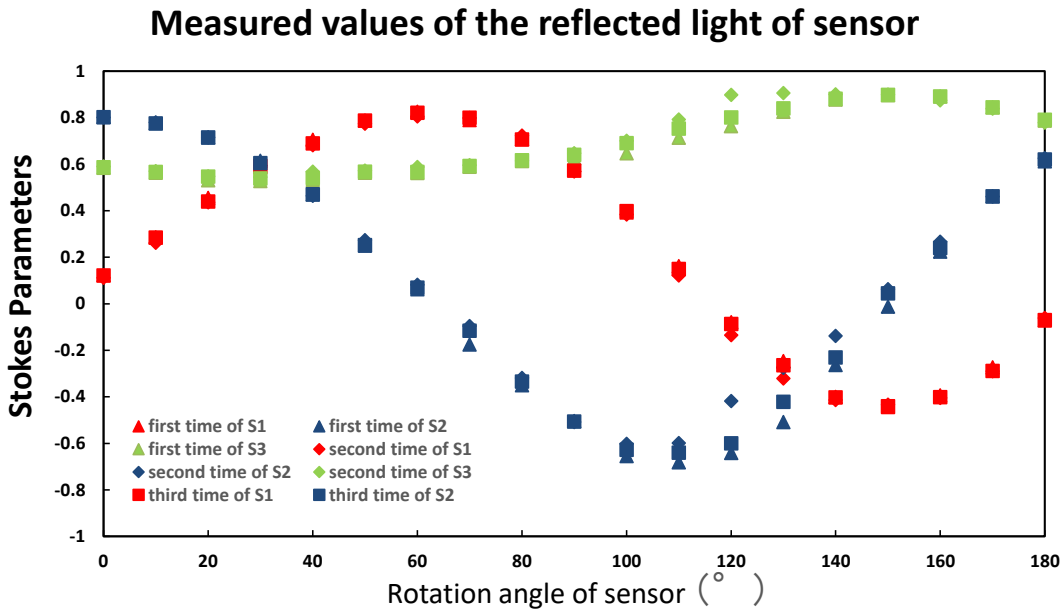

Fig. 5.3.1. The relationship between the polarization states and the rotation angles of the sensor.

In this experiment, we used a neural network to perform data processing to determine the rotation angle of the sensor. The experimental data shown in Fig. 5.3.1 is used as training data and was provided to the neural network for learning, where the measured polarization state was used as the input and the rotation angle of the sensor was used as the output. The feedforward neural network we used is illustrated in Fig. 5.3.2. The error back-propagation is the learning method we used here. Both the time cost and the accuracy of learning results must be considered when operating the learning. Here, the number of neurons in the hidden layer is set to 10, with the neurons denoted as n_1, n_2, ⋯, and n_{10}.

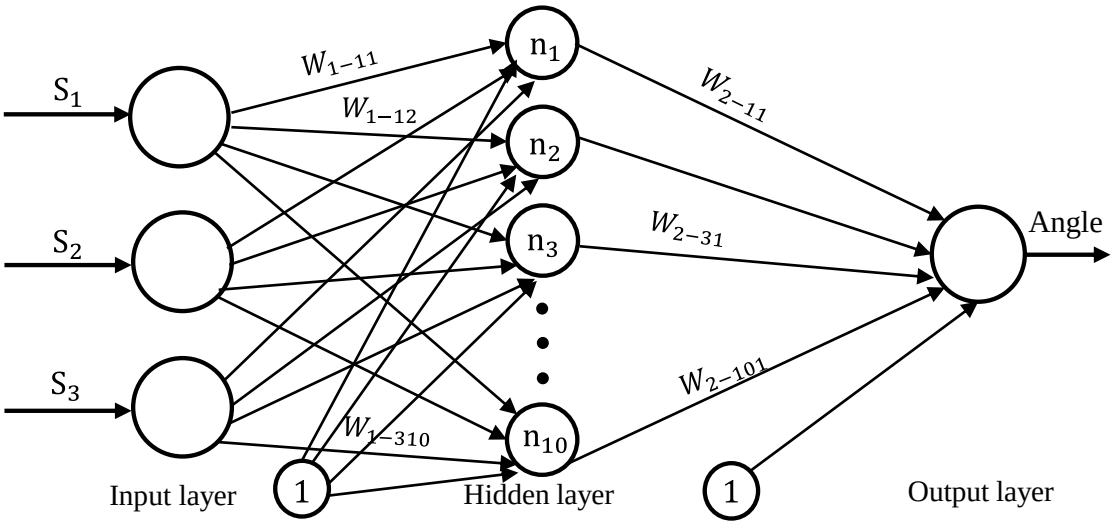

Fig. 5.3.2. Feed-forward neural network used for learning.

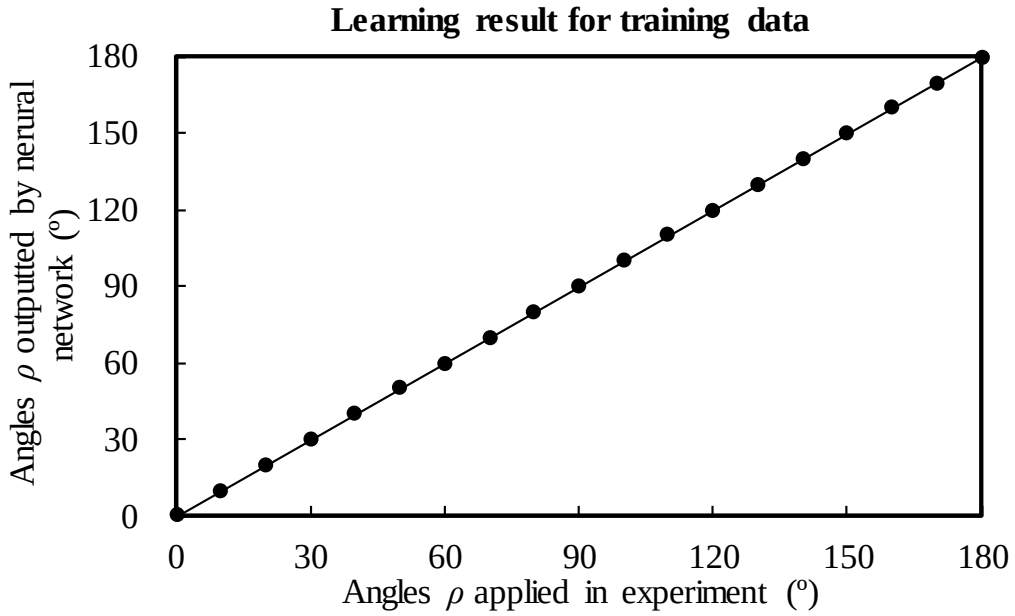

Fig. 5.3.3. Rotation angles of the sensor applied in the experiment and rotation angles outputted by the neural network for training data.

In Fig. 5.3.2, W denotes the weights, and the process of learning is to adjust values of weights to make the output of the neural network infinitely approach the target output. The measured polarization states were provided to the designed neural network and the rotation angles applied in the experiment were provided

to the network as output. During the process of learning, the network is trained to make the output approach the target output, i.e. the rotation angle of sensor applied in the experiment. The number of learning times is 1.26 million, the width of weight correction is 1.0, the gain α is 1.9, and the learning time is 23 seconds. Fig. 5.3.3 shows the comparison between the angles outputted by the designed neural network and the angles actually applied in the experiment [31].

As can be seen from Fig. 5.3.3, the angles applied in the experiment and the angles outputted by the neural network agree very well with each other. Furthermore, the relative errors between them are suppressed to 0.04% or less. This means that the designed neural network was satisfactorily trained and the relationship between the angles applied to the sensor in the experiment and the measured polarization states was correctly determined. When the input is given to the trained neural network, it is expected that the network could yield a correct output corresponding to that input. As shown in Fig. 5.3.1, we measured three times and took three sets of experimental data. In order to test the trained neural network, we used another set of experimental data as test data and provided the polarization state as input to the trained neural network to calculate the angles. The comparison between the calculated angles and the angles that were applied in the experiment, which were used as test data, is shown in Fig. 5.3.4 [31].

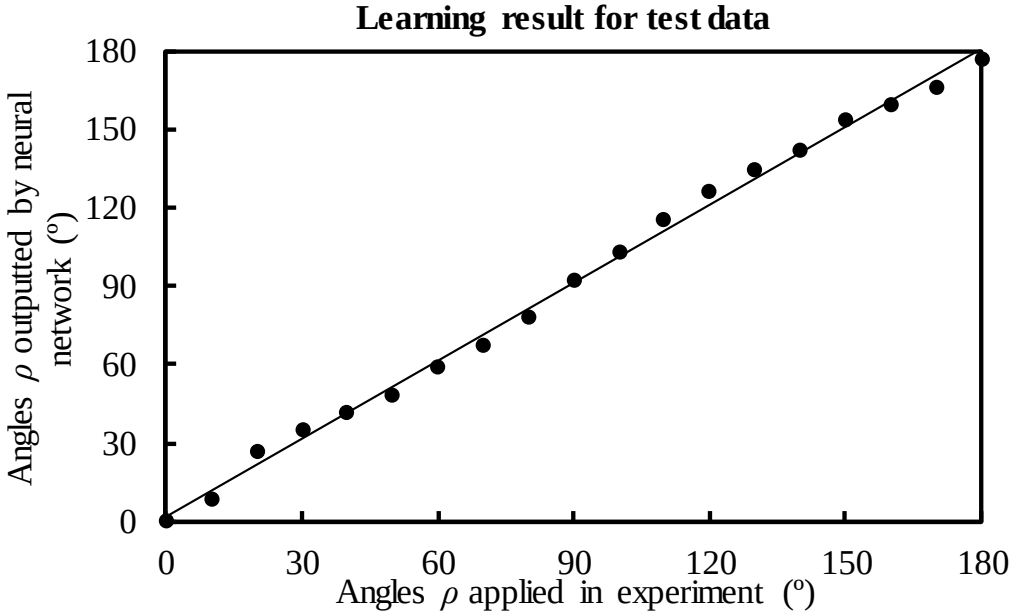

Fig. 5.3.4. Rotation angles of the sensor applied in the experiment and rotation angles outputted by the neural network for test data.

As can be seen from 5.3.4, there is a near-linear relationship between the angles applied in the experiment used as test data and the angles outputted by the trained network. However, an error occurred between the calculated rotation angle and the actual rotation angle at some angles, when the angle is 20º and the interval of 110º to 140º. The errors that occurred are not due to the poor performance of the experimental system, but because we conducted all the experiments manually. In order to eliminate the error of the experimental data due to manual operation as much as possible, we obtained the average values of the first experimental data and the second experimental data, then we used the average values as new training data to perform the learning again. Figure 5.3.5 shows the comparison between the angles outputted by the network and the angles applied in the experiment.

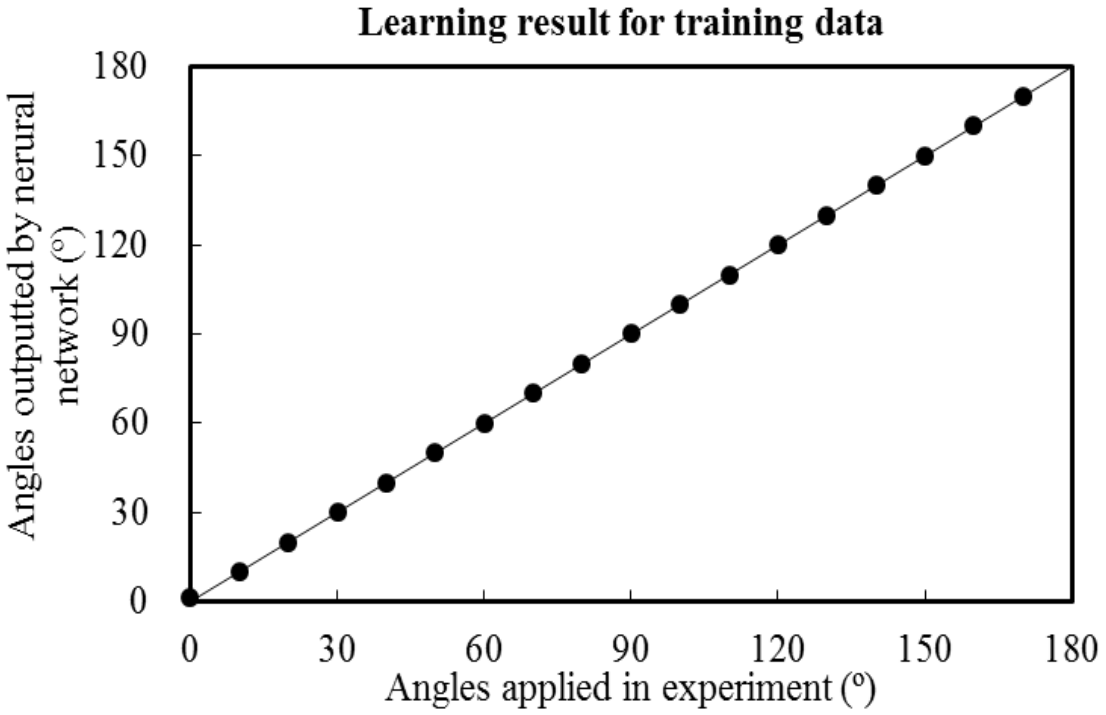

Fig. 5.3.5. Rotation angles of the sensor applied in the experiment and rotation angles outputted by the neural network for new training data.

According to Fig. 5.3.5, the angles applied in the experiment and the angles outputted by the neural network are in very good accordance with each other. The relative errors are suppressed to 0.05% or less. This means that the network was satisfactorily trained and the relationship between the angles applied to the sensor in the experiment and the measured polarization states was correctly determined. In order to test the trained neural network, we provided the third measurement data as test data to the network. The polarization state is provided as input to the network. Figure 5.3.6 shows the comparison between the calculated angles and the angles that were applied in the experiment, which were used as test data.

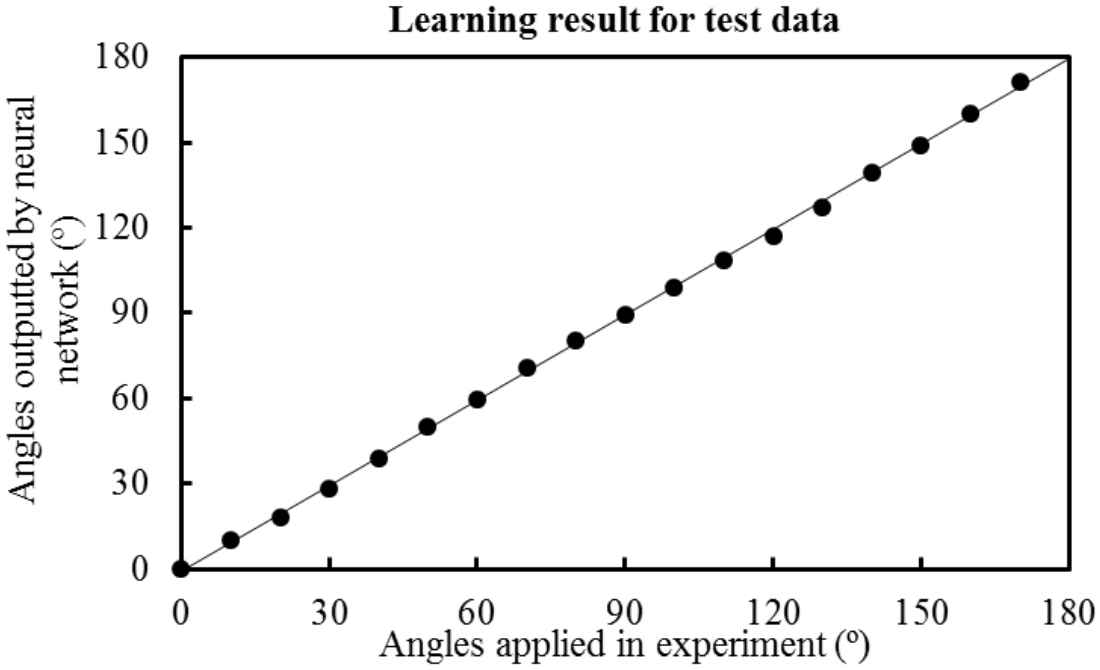

Fig. 5.3.6. Rotation angles of the sensor applied in the experiment and rotation angles outputted by the neural network for new test data.

As can be seen from Fig. 5.3.6, the sensor's rotation angle of the third measured polarization state applied in the experiment and the angle obtained using the trained neural network are very consistent with each other. Since the angles applied in the experiment and the calculated angles are in good agreement, we determined the measurement range to be from 0 to 180º. Then, the strains, which is shown in Fig. 5.3.7, were calculated using the rotation angles in the measurement range with Eq. (3.3.3) and (3.3.4). The measurement range of strains that corresponds to the range of rotation angles is calculated to be 0~2.0×10^5 με. Hence, we can obtain the strains accurately with the proposed measurement method and the data processing method of the neural network.

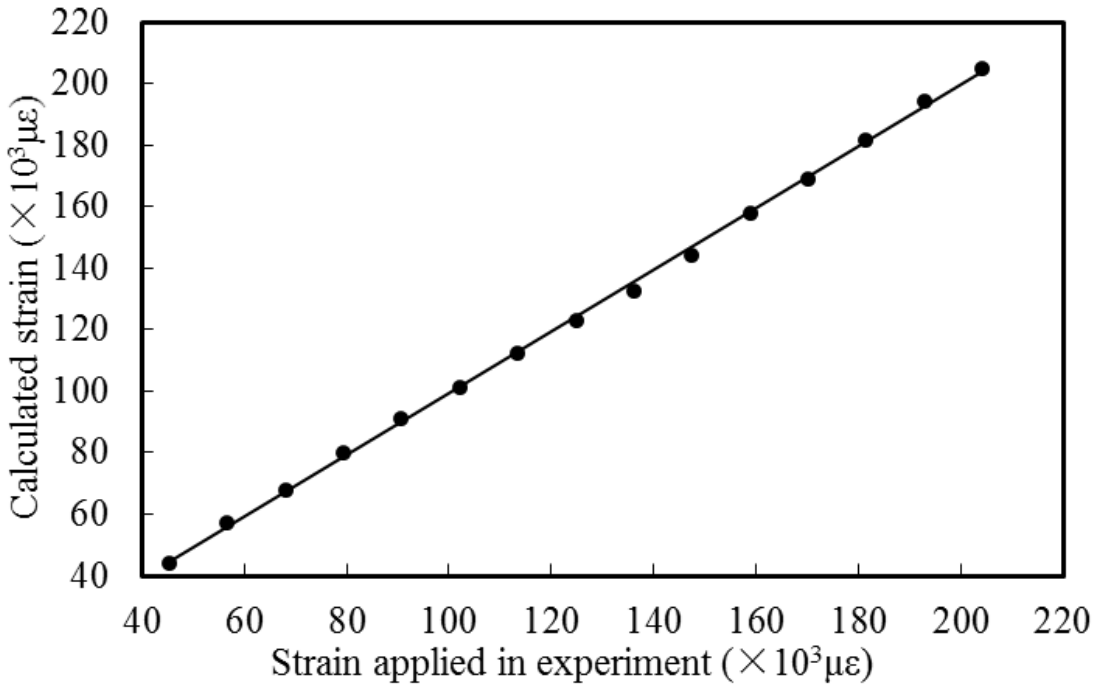

Fig. 5.3.7. Comparison between strains applied in the experiment and calculated strains.

6. Conclusions

6. Conclusions

In the study, we developed a polarization strain sensor system which is low-cost and miniaturized compared with previous polarimetric sensor systems in which the birefringent or high polarization-maintaining fibers are used. In the sensor system, the sensor is a commercially available plain single-mode fiber that is wound into a coil shape, and a laser diode light source and a polarization analyzer are used. In the experiment, the sensor is rotated by pulling the invar wire connected to the sensor. When the sensor is rotated, changes in the polarization state of light transmitting in the fiber is measured using the polarization analyzer. Then, we obtain the rotation angle of the sensor using the movement distance of the invar wire to calculate the strains that were actually applied in the experiment. By comparing the calculated strains and the strains applied in the experiment, we demonstrated that they are in good agreement with each other. The results also verified that the developed sensor system can be used to measure strains. In addition, in order to perform multipoint measurement of strains using the developed sensor system, it is necessary to solve the problems that occur in multipoint measurement. That is, when multiple sensors are connected in series, the front sensor has an effect on the rear sensor. When the first sensor rotates, the polarization of the incident light entering the second sensor changes even if the second sensor does not rotate. This will result in a failure to correctly determine the rotation angles of the second sensor once both sensors are rotated. Moreover, once the two sensors are connected in the experiment, the incident light entering the second sensor cannot be directly measured. To solve this problem, we proposed calculating an arbitrary optical path using the Jones

matrices of two rotated wave plates. When we obtain two Jones matrices representing an optical path, we can calculate the polarization state of the transmitted light of the optical path using the polarization state of the incident light of the optical path. In the experiment, we used the calculated polarization state instead of the actually measured polarization state to obtain the strains applied in the experiment. The measured values of the strains are in good agreement with the calculated values of the strains, and this demonstrated the feasibility of this method using the Jones calculus. In this way, the polarization state of the light entering the second sensor (the polarization state of the transmitted light from the first sensor) can be obtained with the proposed method even if the first sensor rotates when the multipoint measurement is performed. Thus, multipoint strain measurements can be achieved by the proposed method using the time delay of the reflected pulses of a series of sensors.

In this study, we measured the change in the polarization state of the light when the strains were applied. As mentioned before, the polarization state is represented by the Stokes parameters. Thus, a set of strains corresponds to three sets of Stokes parameters. When multiple sensors are connected in series for multipoint measurement, the experimental data will become very huge and it will be very difficult to perform data processing with function fitting. Considering this problem, we decided to use a three-layer feedforward neural network for data processing. We take the polarization state measured in the experiment as input and the rotation angle of the sensor as an output to the neural network. The angles outputted by the designed neural network agree well with the angles applied in the experiment. In order to verify the trained neural network, we use

another set of experimental data as test data and input the polarization state to the trained neural network to calculate its corresponding rotation angle. And the angles outputted by the trained network are almost the same as the angles used as the test data. However, errors occur at some angles. The reason for the errors is considered to be that all experiments were done manually. Then, we performed learning again using the average values of the two sets of experimental data as training data. The third set of data is then provided as test data to the trained network. This time, the rotation angles outputted by the neural network are very consistent with the rotation angles used as the test data. These results verified that we can use the developed sensor system and a neural network for strain measurement. Due to the multi-input and multi-output data processing capabilities of neural networks, we believe that the multipoint measurement of strains can be performed on this basis. As an application of the developed sensor, it is considered to be useful for measuring landslides. In the experiment, we rotated the sensor by pulling the invar wire. Then, if the other end of the invar wire is connected to a stake fixed on the slope, the invar wire will also be pulled when the landslide moves the stake. In this way, it is considered that the extent of the landslide can be determined from the rotation angle of the sensor. Therefore, it is believed that the sensor system developed in this study can be used to detect landslides.

Acknowledgments

First and foremost, I would like to show my deepest gratitude to my supervisor, Associate Professor Shinya Sato, who has provided me with valuable guidance, support, and constant encouragement during the writing of this dissertation as well as in the research. Secondly, I would like to express my thanks to Professor Akira Sakai for his guidance during the weekly seminars and support in the research. Thirdly, I would like to thank Associate Professor Hiroshi Kano for his advice and support in the research. My sincere appreciation also goes to everyone in the laboratory for their support in the research. I also owe my thanks to my friends for their help and advice during the writing of this dissertation. Finally, my sincere gratitude goes to my beloved family for their loving considerations and great confidence in me over the years. This dissertation is dedicated to them all.

References

1. R. Azzam, T. M. Fernandez-steeger, C. Arnhardt, H. Klapperich, K. J. Shou, “Monitoring of landslides and infrastructures with wireless sensor networks in an earthquake environment,” in Proceedings of 5th International Conference on Earthquake Geotechnical Engineering. (2011).
2. R.P. Orense, “Slope failures triggered by heavy rainfall,” Philippine Engineering Journal. Vol.25, pp73-90(2004).
3. R. L. Baum, and J. W. Godt, “Early warning of rainfall-induced shallow landslides and debris flows in USA,” Landslides. Vol.7, pp259-272(2010).
4. T. Uchimura, I. Towhata, L. Wang, S. Nishie H. Yamaguchi, I. Seko, J. Qiao, “Precaution and early warning of surface failure of slops using tilt sensors,” Soils and Foundations. Vol.55, pp1086-1099(2015).
5. C. Pan, X. R. Liu, H. Zhu, X. K. Shan, and X. H. Sun, “Distributed optical fiber vibration sensor based on Sagnac interference in conjunction with OTDR,” Opt. Express. Vol. 25(17), pp20056-20070(2017).
6. T. Nagayama, M. Ruiz-Sandoval, B. F. Spencer Jr, K. A. Mechitov, and G. Agha, “Wireless strain sensor development for civil infrastructure”, Trans. of the Society of Instrument and Control Engineers. Vol. E-3, no. 1, pp.104-109 (2004).
7. A. Kalamkarov, G. Saha, S. Rokkam, J. Newhook, and A. Georgiades, “Strain and deformation monitoring in infrastructure using embedded smart FRP reinforcements”, Composites Part B: Engineering. Vol. 36, no. 5, pp.455-467 (2005).
8. R. Srinivasan, and A. K. Parlikad, “Value of condition monitoring in

infrastructure maintenance", Computers & Industrial Engineering. Vol. 66, no. 2, pp. 233-241 (2013).

9. H.N. Li, D.S. Li, and G.B. Song, "Recent applications of fiber optic sensors to health monitoring in civil engineering", Eng. Struct. Vol.26, pp.1647-1657 (2004).
10. T. H.T. Chan, L. Yu, H.Y. Tam, Y.Q. Ni, S.Y. Liu, W.H. Chung, and L.K. Cheng, "Fiber Bragg grating sensors for structural health monitoring of Tsing Ma bridge: Background and experimental observation", Eng. Struct. Vol.28, pp.648-659 (2006).
11. J.M. Lopez-Higuera, L.R. Cobo, A.Q. Incera, and A. Cobo, "Fiber Optic Sensors in Structural Health Monitoring", J. Lightwave Technol. Vol.29, pp587-608 (2011).
12. R.C. Tennyson, A.A. Mufti, S. Rizkalla, G. Tadros, and B. Benmokrane, "Structural health monitoring of innovative bridges in Canada with fiber optic sensors"Smart mater. struct. Vol.10, pp560 (2001).
13. C.K.Y. Leung, K.T. Wan, D. Inaudi, X. Bao, W. Habel. Z. Zhou, and J.P. Ou, "Review: optical fiber sensors for civil engineering applications", Mater. Struct. Vol.48, pp871-906 (2015).
14. H.N. Li, D.S. Li, and G.B. Song, "Recent applications of fiber optic sensors to health monitoring in civil engineering", Engineering Structures. Vol.26, no.11, pp.1647-1657 (2004).
15. S. Villalba, and J.R. Casas, "Application of optical fiber distributed sensing to health monitoring of concrete structures", Mechanical Systems and Signal Processing. Vol.39, pp.441-451 (2013).

16. D. Luo, Y. Yue, P. Li, J. Ma, L. Zhang, Z. Ibrahim, and Z. Ismail, “Concrete beam crack detection using tapered polymer optical fiber sensors”, Measurement, Vol.88, pp.96-103 (2016).
17. J. Zhao, T. Bao, and U. Amjad, “Optical fiber sensing of small cracks in isotropic homogeneous materials”, Sensors and Actuators A: Physical. Vol. 225, pp.133-138 (2015).
18. R. Unzu, J.A. Nazabal, G. Vargas, R.J. Hernandez, C.Fernandea-Valdivielso, N. Urriza, M. Galarza, and M. Lopez-Amo, “Fiber optic and KNX sensors network for remote monitoring a new building cladding system”, Automation in Construction. Vol.30, pp.9-14 (2013).
19. R. Maaskant, T. Alavie, R. M. Measures, G. Tadros, S. H. Rizkalla, and A. Guha-Thakurta, “Fiber-optic Bragg grating sensors for bridge monitoring”,Cement Concrete Comp. Vol.19, pp21-33 (1997).
20. C. Yang, and S.O. Oyadiji, “Development of two-layer multiple transmitter fibre optic bundle displacement sensor and application in structural health monitoring”, Sensors and Actuators A: Physical. Vol.244, pp.1-14 (2016).
21. K. Lau, C. Chan, L. Zhou, and W. Jin, “Strain monitoring in composite- 76 strengthened concrete structures using optical fibre sensors”, Composites Part B: Engineering. Vol.31, no.1, pp.33-45 (2001).
22. R.C. Jorgenson, and S.S. Yee, “A fiber-optic chemical sensor based on surface plasmon resonance”, Sensors and Actuators B: Chemical. Vol.12, no.3, pp. 213-220 (1993).
23. T. Hu, Y. Zhao, and A. Song, “Fiber optic SPR sensor for refractive index and temperature measurement based on MMF-FBG-MMF structure”, Sensors

and Actuators B: Chemical. Vol.237, pp.521-525 (2016).

24. S.W. James, and R.P. Tatam, “Optical fibre long-period grating sensors: characteristics and application”, Measurement Science and Technology. Vol.14, no.5, (2003).
25. K. Bohnert, J. Nehring, and H. Brandle, “Temperature and vibration insensitive fiber-optic current sensor”, Journal of Lightwave Technology. Vol.20, no.2, pp.267-276 (2002).
26. X. Shu, L. Zhang, and I. Bennion, “Sensitivity characteristics of long-period fiber grating”, Journal of Lightwave Technology. Vol.20, no.2, pp.255-266 (2002).
27. H. E. Joe, H. Yun, S. H. Jo, M. B. G. Jun, and B. K. Min, “A review on optical fiber sensors for environmental monitoring”, Int. J. Pr. Eng. Man-G.T. Vol.5, pp173-191 (2018).
28. C. Shen and C. Zhong, Sens. “Novel temperature-insensitive fiber Bragg grating sensor for displacement measurement”, Actuators A. Vol.170, pp51-54 (2011).
29. J. Chai, Q. Liu, J. Liu, and D. Zhang, “Optical fiber sensors based on novel polyimide for humidity monitoring of building materials”, Opt. Fiber Technol. Vol.41, pp40-47 (2018).
30. Motil, A. Bergman, and M. Tur, “State of the art of Brillouin fiber-optic distributed sensing”, Opt. Laser Technol. Vol.78, pp81-103 (2016).
31. Y. Zhao, L. Yuan, and S. Sato, “Development of a polarization strain sensor system using a neural network”, Jpn. J. of Appl. Phys. Vol.57, 122501 (2018).
32. Y. Zhao, L. Yuan, and S. Sato, “Development of a low-cost and miniaturized

polarimetric optical fiber strain sensor system using Jones calculus", Jpn. J. of Appl. Phys. Vol.58, 012008 (2018).

33. R. Marques, A. Prado, P. Antunes, P. Andre, M. Ribeiro, A. Neto, and M. Pontes, "Corrosion Resistant FBG-Based Quasi-Distributed Sensor for Crude Oil Tank Dynamic Temperature Profile Monitoring", 2015 Sensors. Vol.15, pp30693-30703 (2015).
34. L. Yuan, Y. Zhao, and S. Sato, "Development of a low-cost and miniaturized fiber Bragg gratg strain sensor system", Jpn. J. of Appl. Phys. Vol.56, 052502 (2017).
35. Wang, H. Xiao, J. Wang, Z.Y. Wang, W. Zhao, and R.G. May, "Self-calibrated interferometric-intensity-based optical fiber sensors", J. Lightwave Technol. Vol.19, 1495-1501 (2001).
36. M.N. Armenise, V.M.N. Passaro, F.D. Leonardis, and M. Armenise, "Modeling and design of a novel miniaturized integrated optical sensor for gyroscope systems", J. Lightwave Technol. Vol.19, pp1476-1494 (2001).
37. S. Perez-Garcia and S. Khotiaintsev, "Polarization effects in a fiber optic refractometric sensor with semi-cylindrical plastic detection element", Proc. SPIE 8794, (2013).
38. K. Wada, H. Narui, D. Yakamoto, T. Matsuyama, and H. Horinaka, "Balanced polarization maintaining fiber Sagnac interferometer vibration sensor", Opt. Express. Vol.19, pp21467-21474 (2011).
39. K. Peters, "Polymer optical fiber sensors-a review", Smart Materials and Structures. Vol.20, no.1, (2010).
40. V. Bhatia, and A. M. Vengsarkar, "Optical fiber long-period grating sensors",

Optics Letters. Vol.21, no.9, pp.692-694 (1996).

41. C. Li, and T. Yoshino, “Optical voltage sensor based on electrooptic crystal 75 multiplier”, Journal of Lightwave Technology. Vol.20, no.5, pp.843-849 (2002).
42. T. G. Giallorenzi, J. A. Bucaro, A. Dandridge, G. H. Sigel, J. H. Cole, S.C. Rashleigh, and R.G. Priest, “Optical fiber sensor technology”, IEEE Transactions on Microwave Theory and Techniques. Vol.30, no.4, pp.472-511 (1982).
43. X. Gao, Z. Yin, and N. Song, “Measuring vibration by using fiber Bragg grating and demodulating it by blazed grating”, Chinese Opt. Lett, Vol.2, pp393-395(2004).
44. B. Lee, “Review of the present status of optical fiber sensors”, Opt. Fiber Technol. Vol. 9, pp57-59 (2003).
45. K. T. V. Grattan and T. Sun Dr., “Fiber optic sensor technology: an overview”, Sens. Actuators A. Vol.82, pp40-61 (2000).
46. H. J. Patrick, G. M. Williams, A. D. Kersey, J. R. Pedrazzani, and A. M. Vengsarkar, “Hybrid fiber Bragg grating/long period fiber grating sensor for strain/temperature discrimination”, IEEE Photonic. Tech. Lett. Vol.8, pp1223-1225 (1996).
47. M. Ohn, S. Sandgren, S. Huang, R. Maaskant, R. Stubbe, B. Sahlgren, R. Measures, and H. Storoy, “Phase Based Bragg Intra-Grating Sensing of Strain Gradients”, Proc. SPIE. Vol. 2444, pp. 127-135 (1995).
48. B. Lee, “Review of the present status of optical fiber sensors”, Optical Fiber Technology. Vol. 9, no.2, pp.57-59 (2003).

49. Barrias, J. R. Casas, and S. Villalba, “A Review of Distributed Optical Fiber Sensors for Civil Engineering Applications”, 2016 Sensors. Vol.16, pp748 (2016).
50. R. K. Ramalingam, R. Nast, and H. Neumann, “Fiber Bragg Grating Sensors for Distributed Torsional Strain Measurements in a (RE) BCO Tape”, IEEE Sens. J. Vol.15, 2023-2030 (2015).
51. W. Jin, H. L. Ho, Y. C. Cao, J. Ju, and L. F. Qi, “Gas detection with micro- and nano-engineered optical fibers”, Opt. Fiber Technol. Vol.19, pp741-759 (2013).
52. K. Kyuma, and M. Nunoshita, “Optical fiber sensor ≪ Foundation and application≫”, pp.81-94, (1986), [In Japanese].
53. K. Okoshi, H. Nishihara, K. Okamoto, K. Kyuma, M. Otsu, and K. Hotate, “Optical fiber sensors”, Ohmsha, pp.125-160, (1986), [In Japanese].
54. L. Palmieri, “Distributed polarimetric measurements for optical fiber sensing”, Opt. Fiber Technol. Vol.19, pp720-728 (2013).
55. N. Linze, P. Tihon, O, Verlinden, P. Mégret, and M. Wuilpart, “Development of a multi-point polarization-based vibration sensor”, Opt. Express. Vol.21, pp5606-5624 (2013).
56. X. Dong and H. Y. Tam, Appl. Phys. “Temperature-insensitive strain sensor with polarization-maintaining photonic crystal fiber based Sagnac interferometer”, Lett. Vol.90, 151113 (2007).
57. T. K. Noh and Y. W. Lee, “Temperature-Insensitive Polarimetric Fiber Strain Sensor with Short Polarization-Maintaining Photonic Crystal Fiber”, Appl. Phys. Express. Vol.5, 112502 (2012).

58. Z.Y. Zhang and X. Y. Bao, “Distributed optical fiber vibration sensor based on spectrum analysis of Polarization-OTDR system”, Opt. Express. Vol.16, pp10240-10247 (2008).
59. A.W. Domanski, T.R. Wolinksi, and W.J. Bock, “Method for angular alignment of birefringent fibers in fiber-optic pressure/strain measurement”, IEEE Trans. Instrum. Meas. Vol.41, pp1050-1052 (1992).
60. G. Hegde and A. Asundi, “Performance analysis of all-fiber polarimetric strain sensor for composites structural health monitoring”, NDT & E Int. Vol.39, pp320-327 (2006).
61. T. K. Noh, U. C. Ryu, and Y. W. Lee, “Compact and wide range polarimetric strain sensor based on polarization-maintaining photonic crystal fiber”,Sens. Actuators A-Phys. Vol.213, pp89-93 (2014).
62. https://en.wikipedia.org/wiki/Optical_fiber
63. D. Dennis, “Fiber optic test and measurement”, Prentice Hall PTR, pp. 6-27 (1998).
64. K. Hotate, and H. Murayama, “Introduction to optical fiber sensors”, Photonic Sensing Consortium for Safety and Security, pp. 35-36 (2012), [In Japanese].
65. T. Tsuruoka, “Optical fiber communication: supporting information infrastructure in the multimedia era”, Hitotsubashi Shoten, pp. 36-45 (1997), [In Japanese].
66. K. Okoshi, H. Nishihara, K. Okamoto, K. Kyuma, M. Otsu, and K. Hotate, “Optical fiber sensors”, Ohmsha, pp.5-6, (1986), [In Japanese].
67. K. Hotate, and H. Murayama, “Introduction to optical fiber sensors”, Photonic Sensing Consortium for Safety and Security, pp. 19-20 (2012), [In Japanese].

68. H. Ohno, H. Naruse, M. Kihara, and A.Shimada, “Industrial Applications of the BOTDR Optical Fiber Strain Sensor”, Optical Fiber Technology. Vol.7, pp45-64, (2001).
69. SZ.Yan, and LS. Chyan, “Performance enhancement of BOTDR fiber optic sensor for oil and gas pipeline monitoring”, Optical Fiber Technology. Vol.16, pp100-109, (2010).
70. T. Tadokoro, and I. Akira, “Illustrated Science of Light”, Asakura Shoten, pp.6-22, (2014), [In Japanese].
71. H. Saito, “Basics of optical basics”, Nikkan Kogyo Shimbun, pp.146-152, (2011), [In Japanese].
72. I. Kuwahara, “Field Guide to Polarization”, Optronics sya, pp1-7, (2008), [In Japanese].
73. K. Ono, “Fundamentals and Applications of Polarization Propagation Analysis: Basics of Jaws Calculation Method”, Uchidarokukoho, pp3-18, (2015), [In Japanese].
74. I. Kuwahara, “Field Guide to Polarization”, Optronics sya, pp12-13, (2008), [In Japanese].
75. S. S. Helen, M. P. Kothiyal, and R. S. Sirohi, “Achromatic phase shifting by a rotating polarizer”, Opt. Commun. Vol.154, pp249-254 (1998).
76. Moreno, “Jones matrix for image-rotation prisms”, Appl. Opt. Vol.43, pp3373-3381 (2004).
77. I. Kuwahara, “Field Guide to Polarization”, Optronics sya, pp57-62, (2008), [In Japanese].
78. H. C. Lefevre, “Single-mode fibre fractional wave devices and polarization

controllers”, Electron. Lett. Vol.16, pp778-780 (1980).

79. M. Sakawa, and M. Tanaka, “Introduction to Neurocomputing”, Morikita Publishing Co. Ltd, pp 1-3 (1997), [In Japanese].

80. I. Kumazawa, “Learning and Neural network”, Morikita Publishing Co. Ltd, pp 1-23 (1997), [In Japanese].

81. M. Sakawa, and M. Tanaka, “Introduction to Neurocomputing”, Morikita Publishing Co. Ltd, pp 8-11 (1997), [In Japanese].

82. K. Bahman, “Design and applications of Neural Networks”, Shokodo Publishing Co. Ltd, pp 1-58 (1999), [In Japanese].

83. I. Kumazawa, “Learning and Neural network”, Morikita Publishing Co. Ltd, pp 51-75 (1997), [In Japanese].

84. D. Negrov, I. Karandashev, V. Shakirov, Y. Matveyev, W. Dunin-Barkowski, and A. Zenkevich, “An approximate backpropagation learning rule for memristor based neural networks using synaptic plasticity”, vol. 237, pp.193-82 199 (2017).

85. S. de Montigny, “New approximation method for smooth error backpropagation in a quantron network”, Neural Networks, vol. 60, pp.84-95 (2014).

86. I.A. Basheer, and M. Hajmeer, “Artificial neural networks: fundamentals, computing, design, and application”, Journal of Microbiological Methods, vol. 43, no.1, pp. 3-31 (2000)

87. E.T. Rolls, and S.M. Stringer, “On the design of neural networks in the brain by genetic evolution”, Progress in Neurobiology, vol. 61, no. 6, pp. 557-579 (2000).

88. L. Yuan, “Study on analysis of FBG sensor using neural network”, pp. 42 (2018).